Physics – Uspekhi **50** (7) 705 – 727 (2007) ©2007 Uspekhi Fizicheskikh Nauk, Russian Academy of Sciences

INSTRUMENTS AND METHODS OF INVESTIGATION

PACS numbers: 42.65.Ky, 42.65.Dr, 42.65.Re, 42.65.Wi

Microstructure optical fibers for a new generation of fiber-optic sources and converters of light pulses

A M Zheltikov

DOI: 10.1070/PU2007v050n07ABEH006324

Contents

1. **Introduction** **705**
2. **Photonic-crystal fibers for dispersion and nonlinear-phase-shift compensation in fiber-optic sources of ultrashort light pulses** **708**
   2.1 Designing photonic-crystal fibers for dispersion compensation in a broad spectral range; 2.2 Genetic algorithms for finding the photonic-crystal fiber transverse structure providing the required dispersion profile
3. **Transformation of ultrashort laser pulses in photonic-crystal fibers with a microstructured cladding and a nanostructured core** **711**
4. **Soliton self-frequency shift in photonic-crystal fibers** **713**
5. **Third-harmonic generation by frequency-shifting solitons in a photonic-crystal fiber** **715**
6. **Nonlinear-optical transformation of nanosecond laser pulses and controlled supercontinuum generation in photonic-crystal fibers** **716**
   6.1 Phase matching for four-wave mixing in micro- and nanofibers; 6.2 Nonlinear-optical transformation of nanosecond laser pulses in photonic-crystal fibers
7. **Generation of intense supercontinuum radiation in large-mode-area photonic-crystal fibers** **720**
8. **Hollow photonic-crystal fibers for the soliton delivery of megawatt femtosecond pulses** **722**
   8.1 Hollow photonic-crystal fibers in the nonlinear optics of high-peak-power light pulses; 8.2 Hollow photonic-crystal fibers and soliton delivery of high-peak-power femtosecond pulses; 8.3 Megawatt optical solitons in nonlinear microspectroscopy and laser biomedicine; 8.4 Photonic-crystal fibers with a large hollow core: transmission and transformation of subgigawatt femtosecond laser pulses
9. **Conclusion** **725**
   References **725**

Abstract. **Breakthroughs in microstructure-fiber technologies are pushing the development of a new class of fiber-optic frequency converters, broadband light sources, and short-pulse lasers. The frequency profile of dispersion and the spatial profile of electromagnetic field distribution in waveguide modes of microstructure fibers can be tailored by modifying the core and cladding design on a micro- and nanoscale, suggesting ways of creating novel fiber-optic devices providing the highly efficient spectral and temporal transformation of laser pulses with pulse widths ranging from dozens of nanoseconds to a few optical cycles (several femtoseconds) within a broad range of peak powers from hundreds of watts to several gigawatts. In new fiber lasers, microstructure fibers provide a precise balance of dispersion within a broad spectral range, allowing the creation of compact all-fiber sources of high-power ultrashort light pulses.**

A M Zheltikov Physics Department,
M V Lomonosov Moscow State University, International Laser Center, Vorob'evy gory, 119992 Moscow, Russian Federation
Tel. (7-495) 939 51 74. Fax (7-495) 939 31 13
E-mail: zheltikov@phys.msu.ru

Received 9 January 2007, revised 15 February 2007
Uspekhi Fizicheskikh Nauk **177** (7) 737 – 762 (2007)
Translated by A M Zheltikov; edited by A Radzig

1. Introduction

Modern fiber-optic technologies enable the creation of compact and reliable fiber-format sources and converters of optical signals intended to solve a broad diversity of fundamental and applied problems. Many of the key advantages of fiber laser systems and nonlinear-optical devices originate from the fiber geometry of lasing, amplification, and nonlinear-optical transformation of laser radiation [1]. In fiber lasers, such a geometry provides a high efficiency of pump-to-radiation energy conversion, favorable conditions for heat removal, and high quality of a laser beam spatial profile. Due to large lengths of nonlinear-optical interactions attainable in the waveguide regime [2], compact and efficient fiber-optic components for the control and spectral – temporal transformation of laser pulses can be created using new technologies. Some of these devices, such as fiber-optic compressors, as well as Raman and parametric frequency converters, have already gained wide acceptance in ultrafast optics.

Optical fibers doped with ytterbium or erbium possess a gain band that is sufficient for the generation of ultrashort (femtosecond) laser pulses. However, a number of conceptual

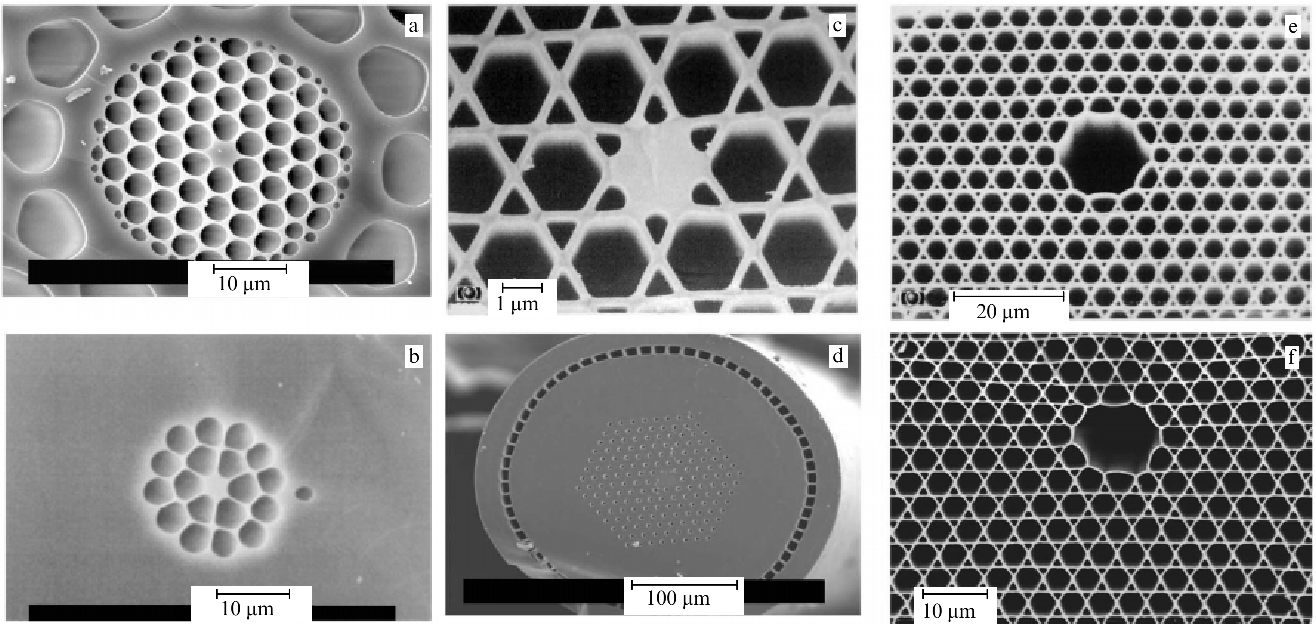

Figure 1. Cross-section images of photonic-crystal fibers: (a – c) fibers with a high optical nonlinearity provided by a small fiber core and a high refractive-index contrast between the core and the cladding, (d) large-mode-area PCF, and (e, f) hollow-core PCFs.

and technical issues have to be resolved to allow the development of practical femtosecond fiber laser sources capable of competing with the available solid-state short-pulse lasers. One of the most serious difficulties impeding the generation of high-power ultrashort light pulses in fiber-optic systems is related to unwanted nonlinear-optical phenomena such as self- and cross-phase modulation, as well as stimulated Raman and Brillouin scattering. These effects induce a nonlinear phase incursion and modify the spectral and temporal structure of the light field, eventually lowering the gain and limiting the bandwidth of the laser output field. The adverse influence of nonlinear-optical effects on the generation, amplification, and transmission of high-power ultrashort light pulses can be reduced through the use of the chirped-pulse amplification (CPA) technique. The CPA concept, which was originally demonstrated for high-power solid-state laser systems in the mid-1980s [3], involves the stretching of a high-power laser pulse before the amplification stage. This allows the peak power of a laser pulse to be lowered at the expense of temporal pulse lengthening. As a result, the influence of nonlinear-optical effects at the amplification stage is substantially reduced. The chirp that a light pulse develops in a stretcher can be compensated for after the amplification with the help of a compressor delivering a high-peak-power ultrashort light pulse. The CPA technique offers a route toward the development of extremely powerful solid-state laser systems [4 – 6].

The development of fiber laser sources of extremely short light pulses, on the other hand, calls for the development of optical fibers that would be capable of precisely balancing the dispersion introduced by all the other components of the fiber laser system. Erbium-fiber technologies, as shown in Refs [7, 8], suggest attractive solutions for the creation of soliton and stretched-pulse femtosecond all-fiber sources of radiation centered at a wavelength of 1.55 μm. However, for fiber laser sources of radiation with wavelengths below 1.3 μm (the wavelength of zero group-velocity dispersion of fused silica) and fiber sources of ultimately short light pulses, the dispersion-compensation technique based on standard fibers fails, necessitating the development of new dispersion-compensating fibers.

In response to this challenge, optical fibers of a new type — microstructure, or photonic-crystal fibers (PCFs)[1] [9 – 13] — are gaining wider application in optical technologies. In their structure, mechanisms of waveguiding, and the properties of guided modes, PCFs differ essentially from standard optical fibers. In PCFs, radiation can be transmitted through either a solid (Figs 1a – 1d) or hollow (Figs 1e, 1f) core surrounded with a microstructured cladding consisting of an array of cylindrical air holes running along the fiber axis. Such a microstructure is usually fabricated by drawing a preform composed of capillary tubes and solid silica rods.

Along with conventional waveguide regimes provided by total internal reflection, PCFs under certain conditions can support guided modes of electromagnetic radiation due to the high reflectivity of their cladding within photonic band gaps (PBGs) [14 – 20]. Such regimes of waveguiding can be supported by fibers with a hollow [14 – 18] or solid [19] core and a two-dimensionally periodic (photonic-crystal) cladding. The high reflectivity provided by the PBGs in the transmission of such a cladding confines radiation in a hollow core, substantially reducing the loss, which is typical of hollow-core-guided modes in conventional, capillary type hollow waveguides and which rapidly grow [21, 22] with a decrease in the diameter of the hollow core.

[1] Strictly speaking, for many of the widely employed microstructure fibers, the periodicity of the cladding and its photonic band gap are unnecessary for the confinement of guided modes in the fiber core. Such fibers may have a nonperiodic cladding exhibiting no photonic band gap. Periodicity of the cladding and photonic band gaps are indeed involved in waveguiding only for a specific class of microstructure fibers. Microstructure fibers could have been thus understood as a broader class of fibers, including PCFs as a subclass. However, according to the tradition arising from to the pioneering work on microstructure fibers [9], motivated by the development of new photonic-crystal structures, the terms 'microstructure fibers' and 'photonic-crystal fibers' are understood here as identical.

The key advantages of PCFs for optical technologies and fiber laser systems are associated with the unique possibility of tailoring the frequency profile of dispersion of waveguide modes in such fibers by modifying the fiber structure [23 – 26]. This allows complicated dispersion profiles unattainable with standard optical fibers to be implemented [26, 27]. As a result, PCFs help in observing novel nonlinear-optical phenomena and new regimes of spectral and temporal transformation of ultrashort laser pulses [27, 28]. Figures 1a – 1c display cross-section images of PCFs with a large difference between the refractive index of the fiber core and the effective index of the fiber cladding. Such a high step of refractive index is induced by a high air-filling fraction of the fiber cladding. Fibers of this type can strongly confine the electromagnetic field in the fiber core, providing high optical nonlinearities, thus radically enhancing nonlinear-optical interactions of light fields at a given peak power of the laser pulse. Highly efficient fiber-format frequency converters of ultrashort light pulses [29] and PCF supercontinuum sources [30 – 34] based on highly nonlinear PCFs (Figs 1a – 1c) are at the heart of advanced systems used in optical metrology [35 – 38], ultrafast optical science [39, 40], laser biomedicine [41], nonlinear spectroscopy [42, 43], and nonlinear microscopy [44 – 46].

The possibility of dispersion tailoring makes PCFs valuable components for dispersion balance and dispersion compensation in fiber-optic laser oscillators intended to generate ultrashort light pulses with a high quality of temporal envelope. Lim et al. [47] have demonstrated an ytterbium-fiber laser source of 100-fs pulses with an energy of about 1 nJ with dispersion compensation based on a PCF instead of free-space diffraction gratings. A highly birefringent hollow-core PCF [48] provides a robust polarization-maintained generation of 70-fs laser pulses with an energy of about 1 nJ in a fiber laser system [49]. Isomäki and Okhotnikov [50] have achieved dispersion balance in an ytterbium femtosecond fiber laser using an all-solid PBG fiber [19]. In contrast to silica – air index-guiding microstructure fibers, including silica and air holes, an all-solid PBG fiber guides light along a silica core surrounded with a two-dimensional periodic lattice of high-index glass inclusions. Dispersion tailoring and a high nonlinearity of small-core PCFs, on the other hand, allow efficient optical parametric oscillation and amplification due to the third-order optical nonlinearity of the fiber material [51 – 53]. Optical parametric oscillators based on PCFs can serve as efficient sources of correlated photon pairs [54, 55].

The maximum laser fluence in an optical system is limited by the laser damage to the material of optical components. An increase in a fiber cross section is a standard strategy for increasing the energy of laser pulses delivered by fiber lasers. [2] Standard large-core-area fibers are, however, multimode [22], making it difficult to achieve a high quality of the transverse intensity profile. This difficulty can also be resolved by using PCFs with small-diameter air holes in the cladding, which filter out high-order waveguide modes [11, 56]. This strategy can provide single-mode waveguiding even for large-core-area fibers [57, 58] (Fig. 1d). A dual-clad PCF design helps to confine the pump field in the microstructured cladding and to optimize a spatial overlap between the pump field and laser radiation. In this type of PCFs, the microstructured part of the fiber is isolated from the cladding by an array of large-diameter air holes (Fig. 1d). Large-mode-area ytterbium-doped PCFs [59, 60] are employed for the creation of high-power lasers [58, 61, 62]. Large-mode-area silica PCFs are also used for the compression of high-power subpicosecond laser pulses [63] and the generation of a supercontinuum with an energy in excess of 1 μJ [64, 65].

The photonic-crystal fiber design presented in Fig. 1a is of special interest for the development of novel fiber-optic sensors [66 – 68]. In sensors of this type, excitation radiation is delivered to an object along the fiber core. The inner part of the microstructured cladding features micrometer-diameter air holes and serves as a high-numerical-aperture collection of the scattered or fluorescent signal from the object, as well as the fiber delivery of this signal to a detector. With such a scheme of sensing, a detector can be placed alongside a radiation source [67, 68]. This fiber design is advantageous for sensing chemical and biological samples by means of one- and two-photon luminescence. A microstructured cladding of PCF can also be conveniently filled with a liquid-phase analyte. Radiation propagating along the fiber core will then induce luminescence of the analyte, allowing the detection of specific types of molecules from the minimal amount of analyte [68]. Such fiber sensors can be integrated into chemical and biological data libraries and data analyzers, including biochips, suggesting an attractive format for the readout and processing of the data stored in such devices.

The energy of laser pulses in fiber-optic devices can be radically increased through the use of hollow-core fibers. For standard, capillary type fibers, however, the loss rapidly grows (as a^{-3}) with a decrease in the core radius a [22, 69]. Because of this problem, such fibers cannot provide single-mode guiding or help to achieve high intensities for pulses with moderate peak powers [18]. The loss of core-guided modes in hollow fibers can be radically reduced if the fiber has a two-dimensionally periodic (photonic-crystal) cladding [11, 15, 17] (Figs 1e, 1f). A strong coupling of incident and reflected waves, occurring within a limited frequency range called a photonic band gap, leads to a high reflectivity of a periodically structured cladding, allowing low-loss guiding of light in a hollow fiber core. [3] Hollow PCF compressors in fiber-laser systems [70, 71] allow the generation of output light pulses with a pulse width on the order of 100 fs in the megawatt range of peak powers.

Thus, PCFs play the key role in the development of novel fiber-laser sources of ultrashort light pulses and the creation of fiber-format components for the control of such pulses. Here, we review the approaches and methods for dispersion engineering of PCFs intended for use in fiber-optic sources of ultrashort light pulses and discuss experiments that demonstrate the potential of PCFs for the highly efficient spectral and temporal transformation of electromagnetic fields with

[2] We distinguish between the geometric area of fiber cross section, viz.

$$S_g = \pi r_{\mathrm{core}}^2 ,$$

where r_{core} is the core radius, and the effective area of a waveguide mode, which is defined as [2]

$$S_{\mathrm{eff}} = \left[\int_{-\infty}^{\infty} \int_{-\infty}^{\infty} \left| F(x, y) \right|^2 \mathrm{d}x \, \mathrm{d}y \right]^2 \left[\int_{-\infty}^{\infty} \int_{-\infty}^{\infty} \left| F(x, y) \right|^4 \mathrm{d}x \, \mathrm{d}y \right]^{-1} ,$$

where $F(x, y)$ is the transverse spatial field profile in the waveguide mode.

[3] For hollow PCFs with a large number of periods in the photonic-crystal lattice in the fiber cladding, the properties of core-guided modes are often largely determined by a few lattice cells that are adjacent to the fiber core. The hollow core does not necessarily have to be at the center of the structure then, suggesting a way of creating fibers with multiple hollow cores.

input pulse widths from dozens of nanoseconds to a few field cycles, and input peak powers ranging from hundreds of watts to several gigawatts.

2. Photonic-crystal fibers for dispersion and nonlinear-phase-shift compensation in fiber-optic sources of ultrashort light pulses

In this section, we examine the potential of PCFs as components providing dispersion balance in fiber systems intended for the generation of high-power ultrashort light pulses, including CPA-based fiber systems. Such systems typically require an accurate compensation for a strong dispersion introduced by a pulse compressor. We demonstrate below in this section that fibers with an unusual dispersion profile are necessary to balance the dispersion introduced by a pulse compressor. It will be shown that the required dispersion profile can be engineered by using PCF technologies.

2.1 Designing photonic-crystal fibers for dispersion compensation in a broad spectral range

The group delay $G_c(\omega)$ introduced by a light pulse compressor can be represented as a Taylor series about the point ω_0 corresponding to the central frequency of the laser pulse delivered by the fiber system:

$$G_c(\omega) = \frac{\partial\varphi_c(\omega)}{\partial\omega} \approx \theta_1 + \theta_2(\omega-\omega_0) + \frac{\theta_3}{2}(\omega-\omega_0)^2 + \frac{\theta_4}{6}(\omega-\omega_0)^3 + \ldots, \qquad (1)$$

where φ_c is the phase shift introduced by the compressor, and $\theta_k = (\partial^k\varphi_c/\partial\omega^k)\big|_{\omega_0}$.

A fiber-optic stretcher should be designed in such a way as to compensate for the group delay (1) within a broad range of frequencies ω, covering the spectrum of an ultrashort laser pulse delivered by the fiber system. Mathematically, this requirement implies minimization of the deviation of the frequency profile of the stretcher-induced group delay $G_s(\omega)$ from the profile of the group delay introduced by the compressor and taken with an opposite sign, $-G_c(\omega)$.

Consider a stretcher consisting of a sequence of M optical fibers supporting waveguide modes with propagation constants $\beta^{(m)}$, $m = 1, 2, \ldots, M$. The group delay introduced by such a stretcher can be written as

$$G_s(\omega) = \sum_{m=1}^{M} G_m(\omega)\,, \qquad (2)$$

where $G_m(\omega)$ is the group delay introduced by the mth fiber with a length l_m.

Expanding $G_m(\omega)$ in a Taylor series about ω_0 yields

$$G_m(\omega) \approx \left[\frac{1}{u_m} + \beta_{2m}(\omega-\omega_0) + \frac{\beta_{3m}}{2}(\omega-\omega_0)^2 + \frac{\beta_{4m}}{6}(\omega-\omega_0)^3 + \ldots\right] l_m\,, \qquad (3)$$

where $u_m = (\partial\beta^{(m)}/\partial\omega)^{-1}_{\omega_0}$ is the group velocity at the frequency ω_0, and $\beta_{km} = (\partial^k\beta^{(m)}/\partial\omega^k)_{\omega_0}$.

As can be seen from Eqns (1)–(3), the overall group delay introduced by the stretcher and the compressor is compensated for with an accuracy up to the qth dispersion order in the absence of a nonlinear phase shift if the stretcher is designed in such a way as to satisfy the following set of $q-1$ linear equations [72]:

$$\sum_{m=1}^{M} \beta_{pm} l_m = -\theta_p\,, \quad p = 2, 3, \ldots, q\,. \qquad (4)$$

With $M = q-1$, the number of unknown variables in this set is equal to the number of equations. A set of equations (4) can then be readily resolved with respect to fiber lengths $l_m^{(1)}$ in the composite stretcher, unless the determinant of the $M\times M$ matrix β_{pm} is equal to zero:

$$\Gamma = \det\beta_{pm} \neq 0\,. \qquad (5)$$

If the condition (5) is satisfied, the solution to set (4) is written down as

$$l_i = \frac{\Gamma_i}{\Gamma}\,, \qquad (6)$$

where

$$\Gamma_i = \begin{vmatrix} \beta_{21} & \ldots & \beta_{2i-1} & -\theta_2 & \beta_{2i+1} & \ldots & \beta_{2M} \\ \beta_{31} & \ldots & \beta_{3i-1} & -\theta_3 & \beta_{3i+1} & \ldots & \beta_{3M} \\ \ldots & \ldots & \ldots & \ldots & \ldots & \ldots & \ldots \\ \beta_{q1} & \ldots & \beta_{qi-1} & -\theta_q & \beta_{qi+1} & \ldots & \beta_{qM} \end{vmatrix} \qquad (7)$$

is the determinant of the matrix obtained from β_{pm} by replacing the ith column in this matrix by the column consisting of the free terms $(-\theta_p)$ in the set of equations (4).

Formally, with $M = q-1$ and $\Gamma \neq 0$, the set of equations (4) can always be resolved with respect to l_m. However, the mathematical solution to set (4) is physically meaningful, i.e., is representative of the lengths of the fibers in the composite stretcher, only if $l_m \geqslant 0$ for all m. This condition is difficult or even impossible to satisfy with a sequence of standard optical fibers.

To illustrate this argument, we consider a typical frequency profile of the group delay (Fig. 2) introduced by a standard grism compressor often used in fiber laser systems [72]. For such a frequency profile of the group delay, we find $\theta_2 \approx -12.45\ \mathrm{ps}^2$, $\theta_3 \approx 6.98\times10^{-2}\ \mathrm{ps}^3$, and $\theta_4 \approx -6.2\times10^{-4}\ \mathrm{ps}^4$ for $\lambda_0 = 1050$ nm, corresponding to the central wavelength of an ytterbium laser. Obviously, the specific

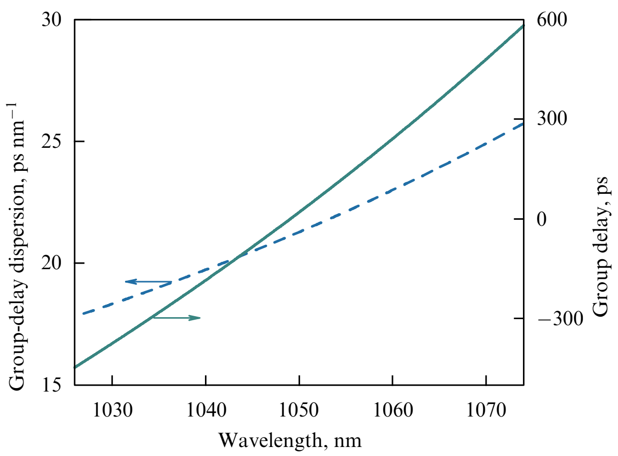

Figure 2. Typical spectral group-delay (solid line) and group-delay dispersion (dashed line) profiles for a grism compressing the fiber-source output.

values of the parameters θ_k can vary depending on the compressor design. However, the signs of these parameters: $\theta_2 < 0, \theta_3 > 0$, and $\theta_4 < 0$ are characteristic of the considered type of a pulse-compressing system.

Suppose that we need to compensate for the compressor-induced group delay with an accuracy up to the third order in dispersion ($q = 3$). To this end, we describe the stretcher dispersion profile in terms of its group-velocity dispersion (GVD) $D = -2\pi c\lambda^{-2}\beta_2$ and third-order dispersion $\beta_3 = \partial^3\beta/\partial\omega^3$. A set of equations (4) is then reduced to two equations ($p = 2, 3$) for two unknown variables each ($M = 2$). The solution to such a set of equations is given by $l_{1,2} = \Gamma_{1,2}/\Gamma$. The considered two-fiber stretcher should have a normal overall GVD. At $\lambda_0 = 1050$ nm, this condition can be readily satisfied with the use of standard optical fibers. The β_{3m} parameter for such fibers is usually positive. With positive β_{pm} ($p = 2, 3$; $m = 1, 2$), the product $l_1 l_2 = \Gamma_1\Gamma_2\Gamma^{-2}$ is always negative for the considered class of group-delay profiles ($\theta_2 < 0$, $\theta_3 > 0$). Consequently, standard fibers cannot compensate for the group-delay introduced by a grism compressor.

Photonic-crystal fibers can be designed in such a way as to provide dispersion profiles unattainable with standard optical fibers. In particular, PCF dispersion can be tailored to achieve the relation between the second- and third-order dispersion coefficients required to compensate for the group delay introduced by a grism compressor in fiber laser–amplifier systems.

The properties of the guided modes of the electromagnetic field in a PCF can be analyzed by applying a fully vectorial localized-function technique [73, 74]. This method involves an expansion of the transverse components of the field $\mathbf{E}(z,t) = \mathbf{E}\exp\left[\mathrm{i}(\beta z - ckt)\right]$ [here, $\mathbf{E} = (E_x, E_y, E_z)$, β is the propagation constant of a waveguide mode, k is the wave number, and c is the speed of light in vacuum] in a set of Gauss–Hermite polynomials. The relevant two-dimensional spatial profile of the refractive index $n^2(x,y)$ in the fiber cross section is expanded in a series in terms of a set of Gauss–Hermite polynomials and trigonometric functions. With such a representation of E_x, E_y, and $n^2(x,y)$, the solution of the vectorial wave equations for the field is reduced to the solution of an eigenfunction and eigenvalue problem of the relevant matrix equation.

Figures 3a–3c present the wavelength dependences of the GVD and the third-order dispersion β_3, calculated with the use of the above-described technique for a silica–air PCF with a cross-section structure shown in the inset to Fig. 3a. The cladding structure of this PCF is parameterized by using the air-hole diameter d and the distance Λ between the centers of the air holes. For sufficiently small Λ, the fiber dispersion features two zero-GVD wavelengths. With large d/Λ ratios, the second zero-GVD wavelength λ_z is tuned within the range of 970–1035 nm by changing the cladding period Λ from 0.77 to 0.80 μm. For radiation wavelengths exceeding λ_z, the considered type of fibers provides normal dispersion ($\beta_2 > 0$, $D < 0$), simultaneously satisfying the requirement $\beta_3 < 0$ needed for the compensation of the group delay introduced by a grism compressor. As shown in Figs 3a–3c, with an appropriate PCF design, dispersion parameters β_2 and β_3 can be optimized for the best compensation of the group delay in the stretcher–compressor system within the required spectral range.

For high-intensity laser pulses, nonlinear-optical processes give rise to nonlinear phase shifts, leading to notice-

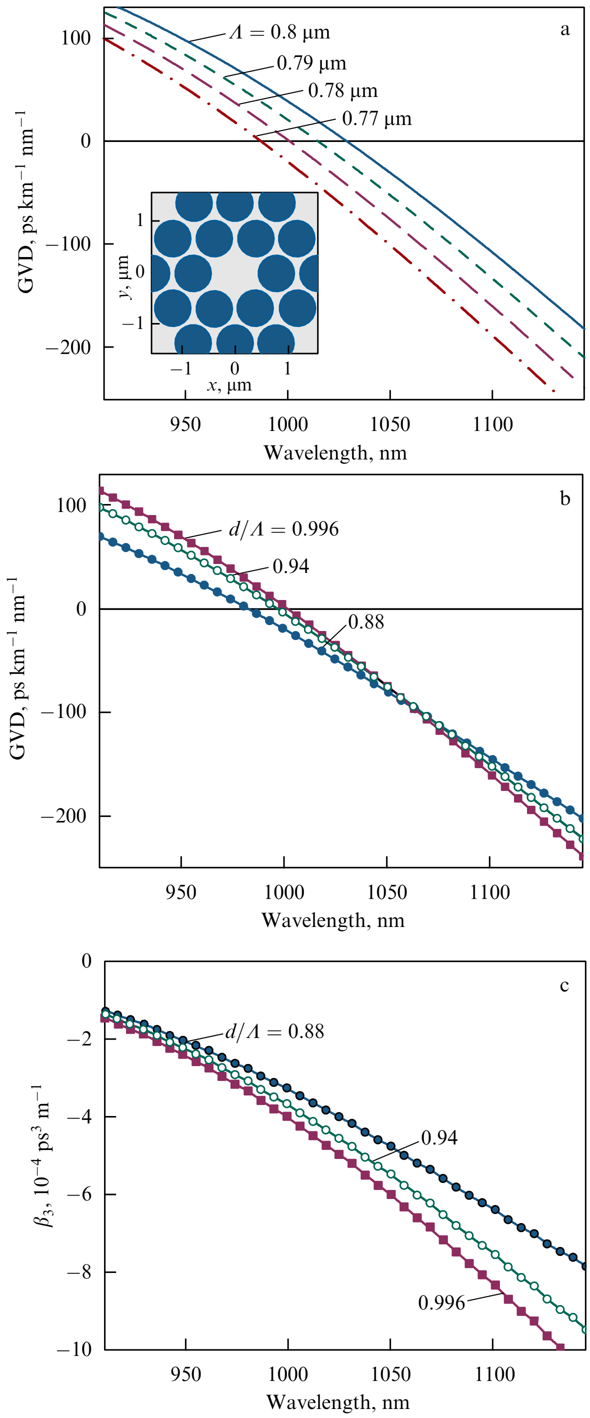

Figure 3. Spectral profiles of the group-velocity dispersion D (a, b) and the third-order dispersion parameter β_3 (c) as functions of the wavelength for a photonic-crystal fiber with the cross-section structure shown in the inset: (a) the pitch of the microstructure cladding Λ varies from 0.77 to 0.80 μm, (b, c) $\Lambda = 0.78$ μm and the d/Λ ratio varies from 0.88 to 0.996.

able distortions of the temporal envelope of the pulse at the output of the fiber system. The influence of nonlinear phase shifts in fiber laser systems can be substantially reduced, as shown by Serebryannikov et al. [72], by optimizing the lengths of the fibers in a composite stretcher on the basis of numerical analysis of pulse evolution in a fiber-optic system including nonlinear-optical effects. According to the approach proposed in Ref. [72], the solution to a set of equations (4) is

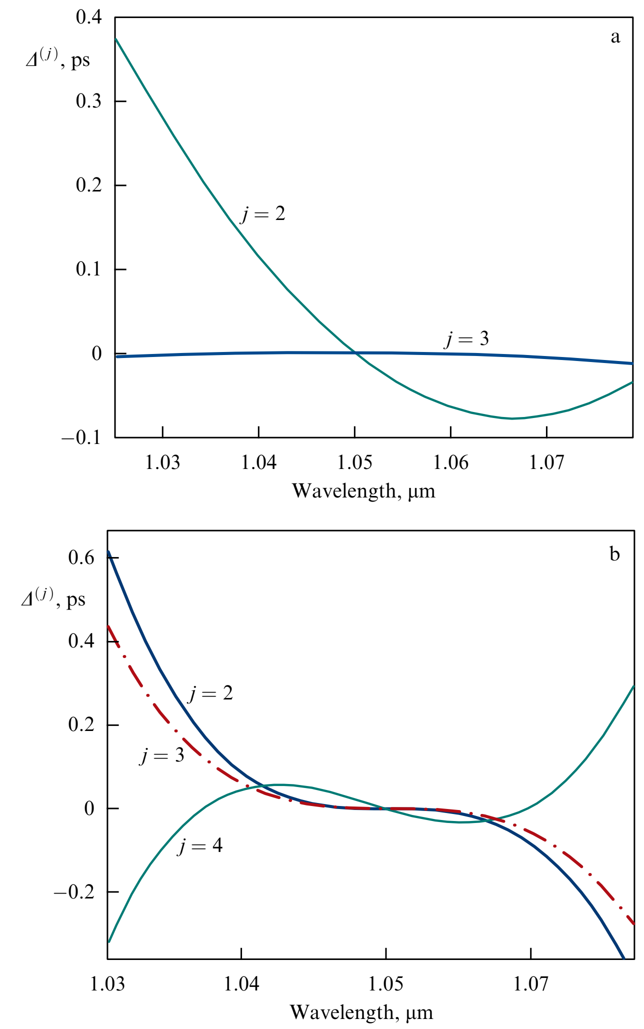

Figure 4. Spectral profile of the uncompensated stretcher – compressor group delay $\Delta^{(j)}$ after the jth step of the iteration procedure minimizing the group delay: (a) the input pulse width is 200 fs, and the input energy is 400 pJ; (b) the input pulse width is 100 fs, and the input energy is 50 pJ.

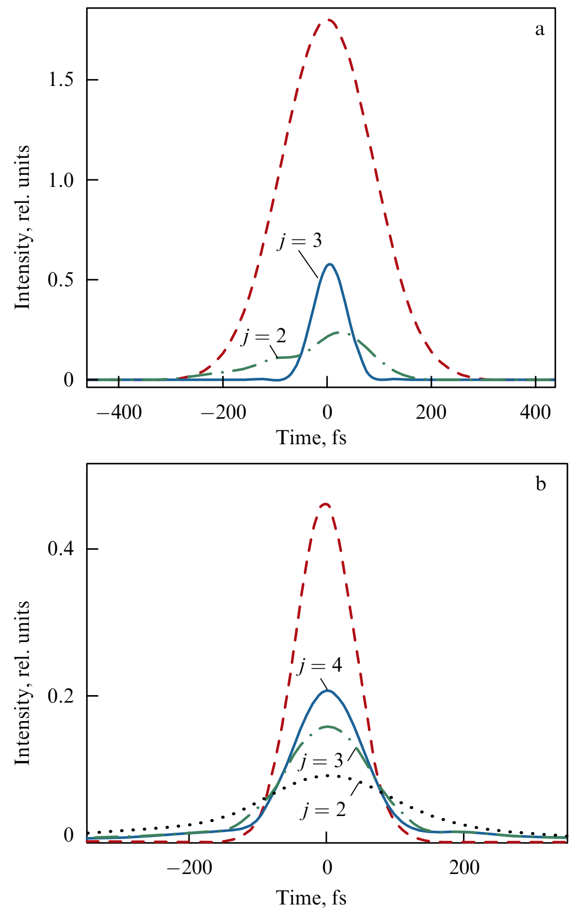

Figure 5. Time-dependent intensity envelope at the output of the stretcher – compressor system after the jth iteration: (a) the input pulse width is 200 fs, and the input energy is 400 pJ; (b) the input pulse width is 100 fs, and the input energy is 50 pJ. The input pulse envelopes are shown by dashed lines.

considered to be the first step of an iterative procedure. Subsequent iterations are intended to determine corrections to the lengths of the fibers in the composite stretcher minimizing distortions in the spectrum and temporal envelope of the output field induced by nonlinear-optical effects. Figures 4a and 4b display a residual (uncompensated) group delay in a fiber stretcher – compressor system after several iteration steps of such a procedure for laser pulses with input pulse widths of 200 and 100 fs, and initial energies of 400 and 50 pJ, respectively. As can be seen from the results presented in these figures, the iteration procedure developed can substantially reduce the residual group delay, thus improving the quality of the temporal envelope of an ultrashort pulse at the output of a fiber stretcher – compressor system (Figs 5a, 5b).

2.2 Genetic algorithms for finding the photonic-crystal fiber transverse structure providing the required dispersion profile

Finding a PCF structure that would provide the required dispersion profile is one of the most important and difficult problems in the design of PCF-based systems for the generation of ultrashort light pulses. For simple PCF structures which can be described in terms of a few parameters, the desired transverse structure can be found by an exhaustive search based on direct dispersion profile calculations for a given refractive-index profile with variable parameters.

The fibers presented in the inset to Fig. 3a and inset 1 to Fig. 6 belong to the class of easily parameterizable structures, as they can be described in terms of the air-hole diameter d and the d/Λ ratio. Parameterization of more complicated PCF structures (see inset 2 to Fig. 6) requires a larger number of parameters. For such structures, finding the PCF profile from the required dispersion profile by an exhaustive search through the solutions to a direct problem becomes problematic. An attractive alternative approach involves the use of genetic optimization algorithms [75].

Genetic algorithms, as shown in Refs [76, 77], suggest a powerful tool for the optimization of PCFs for the minimum deviation from a target dispersion profile within a given class of fiber structures. The genetic-algorithm-based approach developed in Ref. [78] searches for a PCF structure in the class of large-mode-area fibers providing the best group-delay compensation in a fiber stretcher – compressor system. The requirement of a large mode area is of key importance for reducing the nonlinear phase incursion of a light pulse in a fiber system. To illustrate this approach, we consider two types of PCFs with a triangular lattice of air holes in the

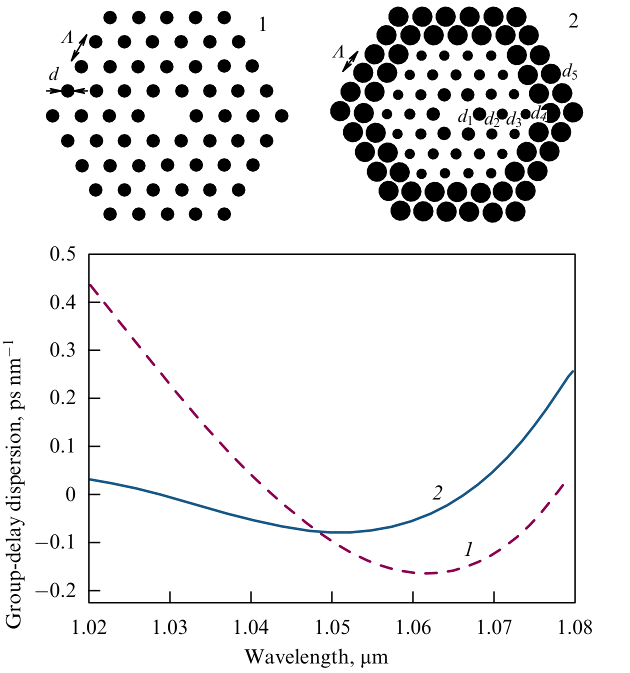

Figure 6. Uncompensated residual group-delay dispersion of a PCF-stretcher – compressor system utilizing 723 m of a first-type PCF (curve *1*) and 345 m of a second-type PCF (curve *2*). The insets display cross-section views of PCFs of the first (1) and second (2) types.

cladding (see the insets to Fig. 6). The fibers are described with a set of parameters $\{d_1, d_2, \ldots, d_N, \Lambda\}$, where d_i are the air-hole diameters. For PCFs of the first type (inset 1 to Fig. 6), all the air holes have the same diameter ($N = 1$). The structure of the fibers of the second type (inset 2 to Fig. 6) is more complicated and is generally described in terms of five different air-hole diameters ($N = 5$). The genetic algorithm implemented in Ref. [78] involves the following sequence of steps. In the first step, a random population of $\{d_i, \Lambda\}_1$ sets is generated, with the parameters d_i and Λ playing the role of genes. Group-velocity dispersion D is calculated for each PCF defined by the set of parameters d_i and Λ using the finite-element method (FEM) [79]. The GVD is then used to find a functional

$$F = \sum_k \left[\Psi(\lambda_k) + l\,D(\lambda_k)\right]^2 , \tag{8}$$

where $\Psi(\lambda)$ is the group-delay dispersion (GDD) introduced by the compressor, l is the PCF length, and k is the summation index which runs through the range of values corresponding to the wavelength interval considered (from 1.02 to 1.08 μm).

The sets of parameters d_i and Λ, corresponding to smaller values of F, are assigned higher survival probabilities and are thus allowed to produce a new generation of individuals, $\{d_i, \Lambda\}_2$, sharing the best features of the individuals of the previous generation. The new generation thus consists of individuals that are better suited for the function considered, defining the first step toward the best set of fiber parameters, corresponding to the optimal PCF. This process is continued as long as each next generation of individuals $\{d_i, \Lambda\}_j$ substantially reduces the functional F with respect to the previous generation. Mutations are introduced through random variations of parameters in a small part of the population in order to prevent the algorithm from converging to a local optimum. Figure 6 presents the wavelength dependences of the residual GDD in a stretcher – compressor system utilizing 723 m of the first-type PCF (curve *1*) and 345 m of the second-type PCF (curve *2*). As can be seen from this figure, the PCF of the second type not only provides a more efficient GDD compensation, but also reduces the loss and weakens nonlinear effects. For 1.05-μm radiation, the effective mode areas for the PCFs of the first and second types are estimated as $S_1 \approx 1.37$ μm^2 and $S_2 \approx 1.43$ μm^2.

3. Transformation of ultrashort laser pulses in photonic-crystal fibers with a microstructured cladding and a nanostructured core

The dispersion and the spatial profiles of PCF modes are usually tailored [23 – 26] by modifying the geometry of the core and the structure of the cladding, as well as by varying the sizes of air holes in the fiber cladding. Theoretical analysis [80 – 84] shows, on the other hand, that control over PCF properties, including dispersion, mode field profiles, and nonlinearity, can be substantially enhanced by modifying the core of a PCF with an array of additional air holes. In recent work [85, 86], this concept has been implemented experimentally. Results presented below in this section suggest that an array of air holes with a diameter of about 500 nm, modifying the core of a PCF, helps to finely tune the frequency dispersion profile and the spatial profile of an electromagnetic field in guided modes of the fiber. This enhanced dispersion and nonlinearity control enables, in particular, a highly efficient frequency conversion of femtosecond Cr:forsterite-laser pulses, yielding frequency-tunable radiation within a wavelength range from 0.45 to 1.0 μm.

A scanning-electron-microscope image of a TF10-glass PCF, employed in experiments [85, 86], is presented in the inset to Fig. 7. The cladding of the fiber has a nearly periodic structure with a pitch of 1.4 μm and an air-hole diameter of 1.2 μm. The central part of the fiber is modified with an array of six air holes with a diameter of about 0.5 μm. The optical nonlinearity of TF10 glass is nearly an order of magnitude higher than the nonlinearity of fused silica which is usually employed for the fabrication of optical fibers. Material

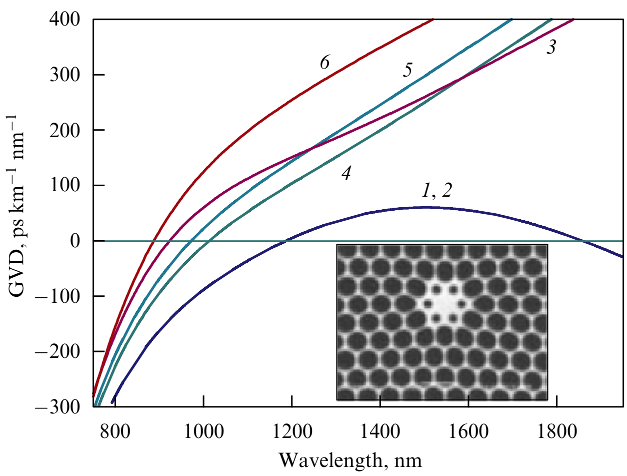

Figure 7. Group-velocity dispersion as a function of the wavelength for the fundamental doublet (*1*, *2*) and higher-order (*3* – *6*) modes of a PCF with a nanostructured core (shown in the inset).

dispersion of TF10 glass also noticeably differs from the dispersion of fused silica. In particular, the zero-GVD wavelength λ_z for this glass ($\lambda_z \approx 2.0$ μm) is red-shifted relative to the zero-GVD wavelength of bulk silica.

The mode properties of nanohole-modified PCFs were analyzed by using the fully vectorial localized-function technique [73, 74] described in Section 2.1. Figure 7 presents the GVD $D = -2\pi c \lambda^{-2} \, \mathrm{d}^2\beta/\mathrm{d}\omega^2$ calculated as a function of radiation wavelength λ for the fundamental and several high-order waveguide modes in the considered type of PCF. From the spatial field distribution in the fundamental mode of the fiber, we derive the following optical nonlinearity coefficient at the wavelength of 1.25 μm: $\gamma \approx 700$ W^{-1} km^{-1}.

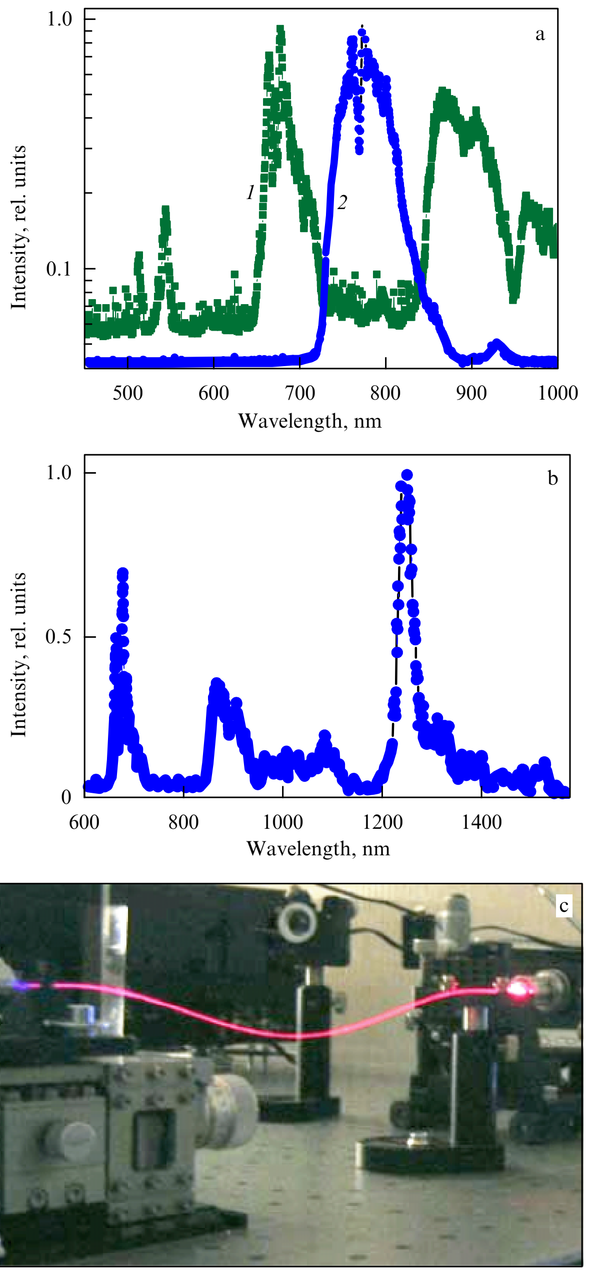

Figure 8. (a) The blue-shifted output of a 20-cm section of a PCF with a nanostructured core. The laser beam is aligned with the fiber axis (*1*) and tilted with respect to the fiber axis (*2*). (b) The spectrum of radiation transmitted through a PCF with a length of 20 cm. The input pulse energy is 2 nJ. The initial pulse width is 70 fs. (c) A view of a PCF with a nanostructured core converting the frequency of femtosecond Cr:forsterite-laser pulses to the visible range.

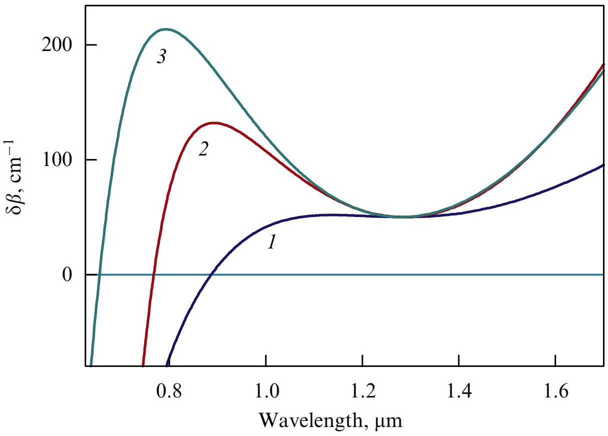

Figure 9. The mismatch $\delta\beta$ between the propagation constant $\beta_s(\lambda_0)$ of a soliton centered at the pump wavelength ($\lambda_0 = 1.25$ μm) and the propagation constant $\beta(\lambda_d)$ of a dispersive wave guided by the fundamental (*1*) and higher-order (*2*, *3*) modes of the PCF calculated as a function of the wavelength λ_d.

Experiments were performed with a long-cavity Cr^{4+}: forsterite laser oscillator [85] pumped by 7.5-W ytterbium-fiber-laser radiation. The Cr:forsterite laser delivered 70-fs pulses with a central wavelength of 1.25 μm and an average power of about 150 mW at a pulse repetition rate of 20 MHz. The central wavelength of Cr:forsterite-laser radiation falls within the region of anomalous dispersion of the PCF (see Fig. 7). Under these conditions, laser pulses tend to form optical solitons as they propagate along the fiber. The retarded part of optical nonlinearity induces a continuous red-shift of these solitons [2]. Additionally, high-order dispersion disturbs the balance between dispersion and nonlinearity and induces the emission of excessive energy of solitons in the form of dispersive waves [87], resulting in the generation of intense radiation in the visible and near-infrared spectral regions (Fig. 8).

The central wavelength of dispersive-wave radiation emitted by a soliton is controlled by the phase matching between the soliton and the emitted dispersive wave. Figure 9 presents the mismatch $\delta\beta = \beta_s(\lambda_0) - \beta(\lambda_d)$ of the propagation constant $\beta_s(\lambda_0)$ of the soliton at the pump wavelength $\lambda_0 = 1.25$ μm and the propagation constant $\beta(\lambda_d)$ of the dispersive wave, calculated as a function of the wavelength λ_d. As can be seen from the comparison of radiation spectra measured at the output of the fiber (see Fig. 8) with the results of calculations (see Fig. 9), the central wavelengths of the most intense spectral components in the PCF output agree very well with the theoretical predictions for the wavelengths satisfying the phase-matching condition $\delta\beta = 0$ between the soliton and the dispersive wave.

Theoretical analysis also prophesies the sensitivity of PCF output spectra to the type of guided mode excited in the fiber (cf. Figs 8 and 9). In experiments, the mode composition of radiation was controlled by changing the tilt angle of the input laser beam with respect to the fiber axis. By varying the input radiation energy and varying the mode composition of radiation propagating through the fiber, it was possible to tune the most intense spectral lines in PCF output spectra in the wavelength range from 0.45 to 1.0 μm.

4. Soliton self-frequency shift in photonic-crystal fibers

The propagation of optical solitons in a medium with retarded nonlinearity is often accompanied by a continuous downshift of the central frequency of the soliton [2, 88, 89]. In the frequency domain, this effect is instructively interpreted as the amplification of the low-frequency part of the soliton spectrum by its high-frequency wing through stimulated Raman scattering. This phenomenon, called soliton self-frequency shift (SSFS), allows the creation of fiber-optic frequency shifters for ultrashort laser pulses. Photonic-crystal fibers substantially enhance SSFS [90–96] due to the strong confinement of the laser field in a small-area PCF core. The unique flexibility of PCF dispersion properties helps in using SSFS for a smooth frequency tuning of low-energy few-cycle pulses [39, 96], offering a new attractive strategy for a reliable synchronization of pump and seed pulses in optical parametric chirped-pulse amplification (OPCPA) [40].

Because of a strong dependence of the SSFS on the parameters of the input pulse, small power fluctuations at the input of the fiber are transformed into unwanted variations of the central wavelength and fluctuations of the delay time of the frequency-shifted soliton at the output of the fiber. This effect limits the accuracy of timing between the frequency-shifted soliton and an ultrashort seed pulse in OPCPA with SSFS-based synchronization [40]. In this section, we show that the SSFS in an optical fiber can be substantially decelerated, following the initial stage of fast frequency shifting. The frequency dependence of the group-velocity dispersion and diffraction-induced increase in the effective mode area in the long-wavelength range give rise to an asymptotic limit of SSFS, controlled by the GVD profile and the frequency dependence of the effective mode area. A PCF is ideally suited for a controlled suppression of SSFS, because the GVD profile and the frequency dependence of the effective mode area can be modified for this type of fiber by fiber structure engineering.

To analyze the dynamics of frequency shifting in a nonlinear medium with retarded nonlinearity, we analyze SSFS using the method proposed by Gordon [97]. This method involves a spectral transformation of the nonlinear Schrödinger equation (NSE)

$$-\mathrm{i}\,\frac{\partial u}{\partial z}=\frac{1}{2}\,\frac{\partial^2 u}{\partial t^2}+|u|^2\,u \tag{9}$$

for the pulse envelope u. The units of time (t_s) and length (z_s) in Eqn (9) are chosen in such a way that

$$\frac{t_s^2}{z_s}=\frac{\lambda^2 D}{2\pi c}=-\frac{\partial^2\beta}{\partial\omega^2}\,, \tag{10}$$

$$P_s z_s=\frac{\lambda A_{\mathrm{eff}}}{2\pi n_2}\,, \tag{11}$$

where λ and ω are the wavelength and frequency, P_s is the soliton power, D is the GVD, β and A_{eff} are the propagation constant and the effective mode area, n_2 is the nonlinear refractive index of the fiber material, and c is the speed of light in vacuum.

The soliton solution to Eqn (9) is written down as $u=\operatorname{sech}(t)\exp(\mathrm{i}z/2)$. The pulse width of such a soliton, defined at the half-maximum of its temporal power profile, is $\tau=1.763t_s$.

Retarded nonlinear response of the medium is included in the model through the following transformation [97, 98] of the nonlinear term on the right-hand side of Eqn (9):

$$|u|^2u\to u(t)\int f(\eta)\,\big|u(t-\eta)\big|^2\,\mathrm{d}\eta\,, \tag{12}$$

where $f(\eta)$ is the real function governing the Raman response of the fiber material. Fourier transform of this function recovers the optical susceptibility of the medium:

$$\chi(\Omega)=\int f(\eta)\exp(\mathrm{i}\Omega\eta)\,\mathrm{d}\eta\,,$$

and the imaginary part of this susceptibility, in turn, controls the Raman gain $\alpha_R(\Omega)=2\,\mathrm{Im}\,\chi(\Omega)$.

Spectral transformation of Eqn (9) with regard to the replacement (12) yields the following relationship for the SSFS rate expressed in THz km^{-1} [97]:

$$\frac{\mathrm{d}\nu}{\mathrm{d}z}\approx-\frac{\mu\lambda^2 D}{t_s^3}\int_0^\infty\frac{\Omega^3 R(\Omega/2\pi t_s)}{\sinh^2(\pi\Omega/2)}\,\mathrm{d}\Omega\,, \tag{13}$$

where μ is a factor, and $R(\Omega/2\pi t_s)=\alpha_R(\Omega)$.

A linear approximation of the function $R(\xi)$ [$R(\xi)\approx 0.492\,\xi/13.2$ for fused silica] gives the central expression of the Gordon model, allowing calculation of the SSFS rate $\mathrm{d}\nu/\mathrm{d}z$ [97]:

$$\frac{\mathrm{d}\nu}{\mathrm{d}z}\approx-\frac{\kappa_G}{\tau^4}\,, \tag{14}$$

where $\kappa_G=\kappa_0\lambda^2 D$ is a constant coefficient in the Gordon model. For $\lambda=1.5$ μm, $D=15$ ps km^{-1} nm^{-1}, Eqn (14) gives[4] $\mathrm{d}\nu/\mathrm{d}z\approx-0.0436/\tau^4$.

The Gordon formula played the key role in identifying significant tendencies of SSFS and in explaining interesting aspects of this phenomenon. Photonic-crystal fibers can radically enhance nonlinear-optical interactions, providing wavelength shifts of 600–700 nm within propagation lengths of 15–20 cm [90–96]. For such fibers, several important physical factors leading to deviations from the Gordon formula have to be taken into consideration. Numerical analysis of the generalized NSE, including the retarded optical nonlinearity (the Raman response of the medium), indicates a deceleration of the frequency shifting of a soliton [99, 100], as well as an ultrashort pulse of a more general form [101] in a certain phase of pulse propagation in a fiber. Numerical simulations performed in Refs [99, 100, 102, 103] directly demonstrate the deceleration of SSFS induced by the frequency dependence of the effective mode area in a fiber. For practical applications of SSFS, the key issue is to reduce the sensitivity of the SSFS and the delay time of the frequency-shifted soliton to the parameters of the input pulse. Solving this problem calls for a careful analysis of the physical factors decreasing the SSFS rate compared to the frequency-shifting rate dictated by the Gordon formula (14).

To analyze physical factors that can suppress the SSFS in an optical fiber, we use Eqns (10) and (11) to rewrite formula

[4] We give this expression in the original notation introduced by Gordon [97]. The numerical factor appearing in this formula is measured in units of s^3 km^{-1}.

(14) as

$$\frac{\mathrm{d}\nu}{\mathrm{d}z} \approx -\frac{0.104\kappa_0}{\lambda^4 A_{\mathrm{eff}}^2 D} \,. \tag{15}$$

Apart from the explicit wavelength dependence, Eqn (15) comprises the GVD and the effective mode area, which change because of high-order dispersion and diffraction, respectively, as the central frequency of the soliton is shifted due to the Raman effect. Guided modes are typically more compact for short wavelengths and are characterized by a large effective area in the long-wavelength range. For PCFs, the $A_{\mathrm{eff}}(\lambda)$ dependence is controlled by the structure of the fiber cross section. In a broad class of PCFs, this dependence is quite strong (Fig. 10a). Below, we demonstrate that the wavelength dependence of the effective mode area is often the key physical factor decelerating the SSFS.

For a qualitative analysis of the wavelength dependences of the GVD and the effective mode area, we express D through $\beta_2 = \partial^2\beta/\partial\omega^2$: $D = -(2\pi c/\lambda^2)\,\beta_2$, and represent the parameters appearing in the denominator in Eqn (15) as Taylor series about the wavelength λ_0:

$$\lambda^2 \approx \lambda_0^2\left(1 - \frac{2\lambda_0}{c}\,\nu\right), \tag{16}$$

$$A_{\mathrm{eff}}^2 \approx A_0^2(1 - 2\alpha\nu)\,, \tag{17}$$

$$\beta_2 \approx \beta_{20}\left(1 - \frac{2\pi\beta_{30}}{|\beta_{20}|}\,\nu\right), \tag{18}$$

where $A_0 = A_{\mathrm{eff}}(\lambda_0)$, $\alpha = -A_0^{-1}(\partial A_{\mathrm{eff}}/\partial\nu)|_{\lambda=\lambda_0}$, and $\beta_{30} = \partial^3\beta/\partial\omega^3|_{\lambda=\lambda_0}$ is the third-order dispersion coefficient. In view of the wavelength dependence of the effective mode area, the coefficient α in the expansion for A_{eff} is defined in such a way that $\alpha > 0$. In writing the power series for β_2, we kept in mind that the condition $\beta_2 < 0$ is necessary for soliton formation.

Substituting the power series (16)–(18) into equation (15), we arrive at

$$\frac{\mathrm{d}\nu}{\mathrm{d}z} \approx -\frac{\kappa_{\mathrm{G}}}{\tau^4}\,(1 + \theta\nu)\,. \tag{19}$$

Here, the following notation was used:

$$\theta = 2\left(\frac{\lambda_0}{c} + \alpha + \psi\right), \tag{20}$$

where $\psi = \pi\beta_{30}/|\beta_{20}|$.

Integration of Eqn (19) yields the following expression for the soliton frequency shift:

$$\nu(z) = \frac{1}{\theta}\left[\exp\left(-\theta\,\frac{\kappa_{\mathrm{G}}}{\tau^4}\,z\right) - 1\right]. \tag{21}$$

In the regime where $\theta\kappa_{\mathrm{G}}\tau^{-4}z \ll 1$, expression (21) is reduced to the Gordon formula (14). However, as the soliton propagates further along the fiber, its frequency shift is decelerated. Expression (21) suggests the existence of the upper bound for the SSFS: with $\theta\kappa_{\mathrm{G}}\tau^{-4}z \gg 1$, we find that $\nu(z) \to -\theta^{-1}$.

As can be seen from Eqns (20) and (21), SSFS deceleration is caused by a gradual variation of local soliton parameters. As the soliton propagates along the fiber, its central wavelength is shifted, leading to changes in the GVD and the effective mode area. To quantify the impact of each of these factors on the SSFS, we introduce the following spatial scales: $l_\lambda = c\tau^4(2\lambda_0\kappa_{\mathrm{G}})^{-1}$, $l_\alpha = \tau^4(2\alpha\kappa_{\mathrm{G}})^{-1}$, and $l_D = \tau^4|\beta_{20}|(2\pi\beta_{30}\kappa_{\mathrm{G}})^{-1}$. Figure 10a displays characteristic wavelength dependences of the effective mode area and the GVD

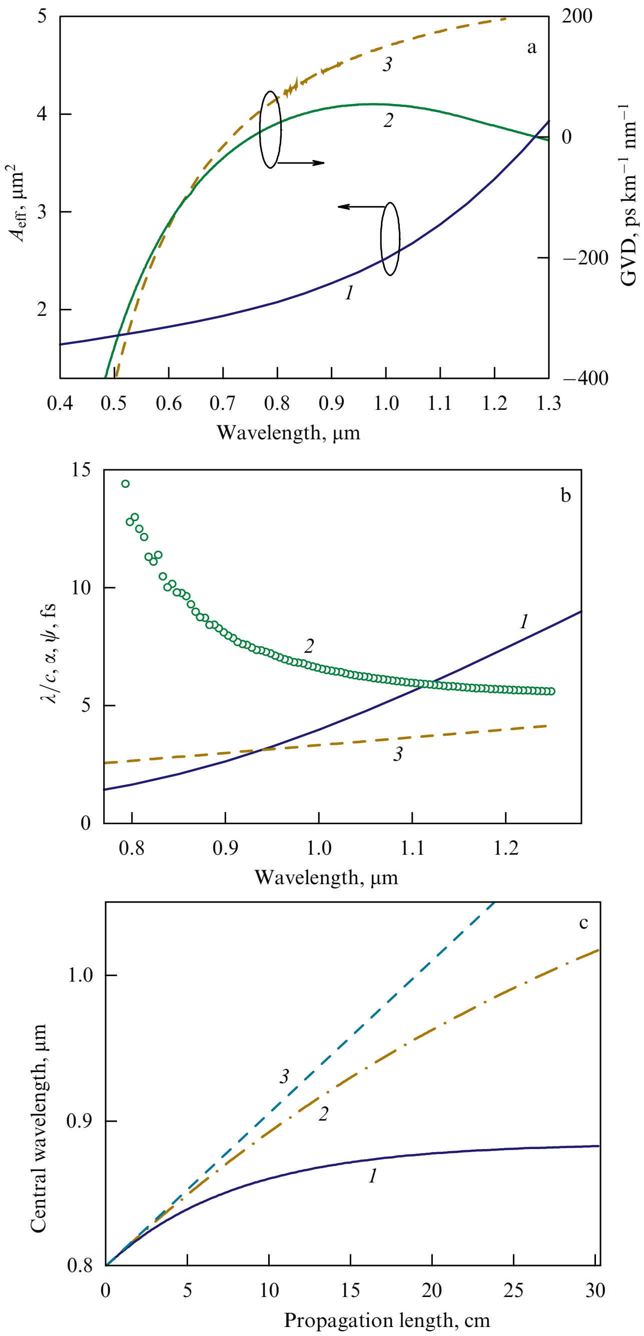

Figure 10. (a) Wavelength dependences of the effective mode area (line *1*) and group-velocity dispersion (lines *2*, *3*) typical of a fused silica photonic-crystal fiber. (b) Wavelength dependences of the parameters α (*1*), ψ (*2*), and λ/c (*3*) for an optical fiber with the $A_{\mathrm{eff}}(\lambda)$ and dispersion profiles shown by lines *1* and *3*, respectively, in Fig. 10a. (c) The central wavelength of a soliton as a function of the propagation length of the soliton in a medium with a retarded nonlinear-optical response for different regimes of soliton self-frequency shift: (*1*) $l_\alpha = 10$ cm and $l_\lambda = 37$ cm; (*2*) $\alpha = 0$ and $l_\lambda = 37$ cm, and (*3*) $\theta \neq 0$.

for PCFs [39, 40, 95, 96, 104]. As the wavelength is shifted from 0.8 to 1.3 μm (a typical SSFS for 6-fs laser pulses in experiments [40]), the effective mode area, as shown by line *1* in Fig. 10a, can increase by a factor of more than two. The GVD profile of PCFs can be modified by changing the cross-section structure of the fiber. Curves *2* and *3* in Fig. 10a represent two GVD profiles typical of PCFs. In the first case (curve *2*), the structure of a PCF provides two zeros in the GVD profile, which bound the spectral range where solitons can exist. In the second case (curve *3*), the GVD changes from 63 to 210 ps km^{-1} nm^{-1} as the wavelength is shifted from 0.8 to 1.3 μm. This GVD change may have a considerable influence on the SSFS rate.

Figure 10b presents the wavelength dependences of the parameters ψ, α, and λ/c, which control, in accordance with Eqns (20) and (21), the SSFS rate. It can be seen from these plots that high-order dispersion is the main factor that limits the soliton frequency shift at the initial stage of SSFS. As the soliton is shifted toward longer wavelengths, the diffraction mechanism starts to play an increasingly important role, becoming a dominant factor of SSFS suppression in the near-IR range (for $\lambda > 1.1$ μm in Fig. 10b).

Figure 10c illustrates SSFS deceleration induced by changes in the central wavelength of the soliton and the wavelength dependence of the effective mode area. The central wavelength of the input laser pulse is taken equal to 800 nm. With typical parameters of a fused silica PCF, viz. $D \approx 25$ ps $\text{km}^{-1}\,\text{nm}^{-1}$, $A_0 \approx 2.1\ \mu\text{m}^2$, $n_2 \approx 3\times10^{-16}\ \text{cm}^2\,\text{W}^{-1}$, we find $\kappa_G \tau^{-4} \approx 5$ THz cm^{-1}. Under these conditions, $l_\lambda \approx 37$ cm. For the wavelength dependence of the effective mode area presented by curve *1* in Fig. 10a, we have $l_\alpha \approx 10$ cm. Curve *1* in Fig. 10c shows how the central frequency of the soliton would have changed with the above-specified values of l_λ and l_α if the GVD was constant. Suppression of SSFS becomes noticeable within a typical length $l_s = (l_\alpha^{-1} + l_\lambda^{-1})^{-1} \approx 8$ cm. The assumption of a constant mode area, on the other hand, gives $l_s = l_\lambda \approx 37$ cm. In this regime, the tendency for SSFS deceleration becomes noticeable within much larger fiber lengths (curve *2* in Fig. 10c).

If variations in the local parameters of a wavelength-shifted soliton are neglected, the Raman effect leads to an infinite growth in the central wavelength of the soliton (curve *3* in Fig. 10c). In this regime, the central wavelength of the soliton at the output of the fiber is especially sensitive to small power fluctuations of the input laser pulse. Luckily, SSFS suppression induced by high-order dispersion and the wavelength dependence of the effective mode area reduces unwanted variations in the central wavelength and the delay time of the frequency-shifted soliton with respect to the input pulse. This circumstance improves the precision of time synchronization of pump and seed pulses in OPCPA with the use of solitons frequency-shifted in PCFs [40].

5. Third-harmonic generation by frequency-shifting solitons in a photonic-crystal fiber

Third-harmonic generation (THG) is one of the basic nonlinear-optical phenomena [105]. This effect is widely used to upconvert the frequency of laser radiation and serves as a tool for nonlinear-optical spectroscopy and microscopy, providing valuable information on the properties of materials and fast processes in physical, chemical, and biological processes [106, 107]. Photonic-crystal fibers allow observation of new, unusual regimes of THG [108–116]. Ultrashort light pulses propagating in PCFs in the regime of anomalous dispersion tend to form optical solitons which undergo a continuous red shift due to the retarded part of the optical nonlinearity of the fiber material (see Section 4 of this review). These frequency-shifting solitons can serve as a pump field for the THG process [117]. For fibers that provide multimode waveguiding in the short-wavelength range, the continuously shifting soliton frequency sweeps over a sequence of phase-matching resonances with waveguide modes of the third-harmonic field. As a consequence, the spectrum of the third harmonic at the output of the fiber displays a series of intense peaks whose central frequencies noticeably differ from the triple input pump-field frequency [118, 119].

The THG efficiency reaches its maximum when the pump field is phase-matched with the third-harmonic field. Since the dispersion of a soliton lies away from the dispersion of a linear dispersive wave with the same frequency, phase-matching conditions for THG by a soliton pump field (similar to phase-matching conditions for general type soliton–dispersive-wave four-wave mixing [120–122]) differ from the phase-matching conditions for all-dispersive-wave THG. To analyze phase matching between a soliton pump field and a nonsoliton (dispersive-wave) third-harmonic field, we represent the soliton pump field in the following form

$$A = \psi(\xi) \exp\left\{-\mathrm{i}\omega_s t + \mathrm{i}\left[\beta_n(\omega_s) + q\right] z\right\}. \tag{22}$$

Here, $\xi = t - z/v_g$ is the time in the retarded frame of reference, β_n is the propagation constant of the nth waveguide mode, z is the longitudinal coordinate along the direction of field propagation, ω_s and v_g are the central frequency and the group velocity of the soliton, $\psi(\xi)$ is the temporal envelope, $q = \gamma P/2$, γ is the optical nonlinearity coefficient, and P is the peak power.

The Fourier transform of the field A is written as

$$A = \int \widehat{F}(\omega) \exp\left\{-\mathrm{i}(\omega_s - \omega)t + \mathrm{i}\left[\beta_n(\omega_s) + q - \frac{\omega_s - \omega}{v_g}\right] z\right\} \mathrm{d}\omega\,, \tag{23}$$

where $\widehat{F}(\omega)$ is the spectrum of the soliton, and

$$\beta_{\text{sol}}(\omega) = \beta_n(\omega_s) + q + \frac{\omega - \omega_s}{v_g} \tag{24}$$

is the propagation constant of the soliton (see also Refs [87, 117, 123]).

The mode index of the third-harmonic field is defined as $n_m(3\omega) = \beta_{\text{TH}}(3\omega)\,c/3\omega$, where $\beta_{\text{TH}}(3\omega) = \beta_m(3\omega)$ is the propagation constant of the mth waveguide mode at the third-harmonic frequency. The phase-matching condition for the THG process is then written down as follows:

$$n_m(3\omega) = n_{\text{sol}}(\omega)\,, \tag{25}$$

where $n_{\text{sol}}(\omega) = \beta_{\text{sol}}(\omega)/k$ is the effective mode index of the soliton, $k = 2\pi/\lambda$, and λ is the wavelength.

Figures 11a and 11b display the results of experiments [119], illustrating some of the significant properties of THG by a soliton pump in a PCF. In these experiments, femtosecond Cr:forsterite-laser pulses with an input spectrum shown by the dashed line in Fig. 11a are launched into a PCF with a cross-section structure presented in the inset to the same

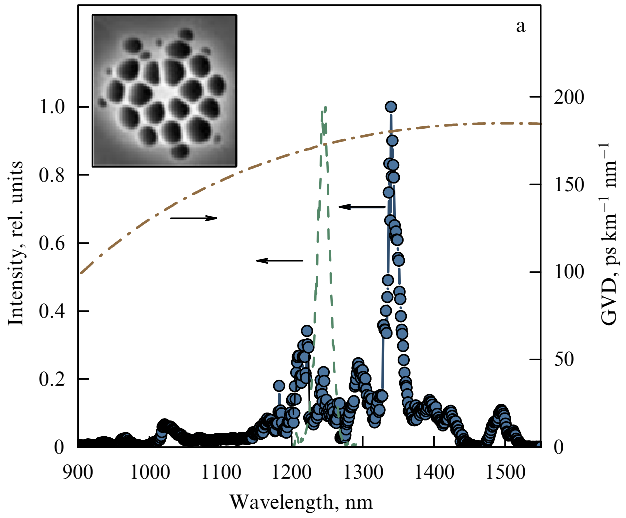

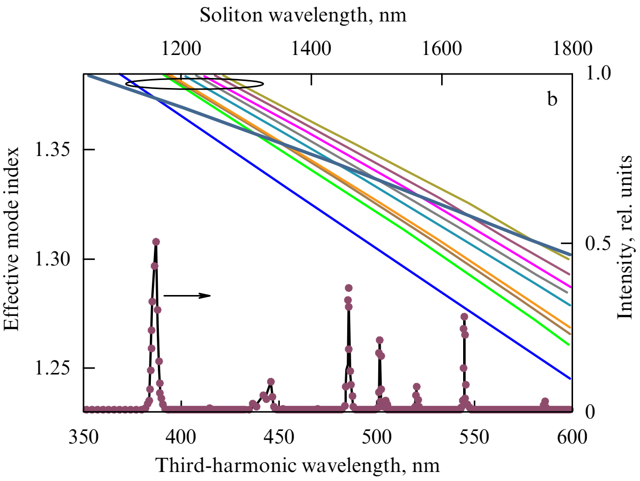

Figure 11. (a) The spectral profile of the group-velocity dispersion (dot-and-dash line) for the fundamental mode of the PCF shown in the inset. The spectrum of the input femtosecond Cr:forsterite-laser pulse is shown by the dashed line. The spectrum of laser pulses transmitted through a 12-cm PCF is presented by filled circles connected by a solid line. The input pulse energy is 0.5 nJ. (b) Spectrum of the third harmonic (filled circles connected by a solid line) generated in a 30-cm PCF by 2-nJ 120-fs Cr:forsterite-laser pulses. The bold line shows the effective mode index $n_{\rm sol}$ of the soliton pump in the fundamental PCF mode as a function of the wavelength. The fine solid lines show the effective mode indices n_m of high-order PCF modes as functions of radiation wavelength.

figure. The dot-and-dash line in Fig. 11a represents the GVD profile for this fiber. The central wavelength of Cr: forsterite-laser radiation falls within the range of anomalous dispersion of the PCF. The laser pulses evolve toward solitons as they propagate through the fiber. The retarded optical nonlinearity of the fiber induces a continuous red shift of the soliton. For a piece of PCF with a length of 12 cm and an input pulse energy of 0.5 nJ, the spectrum of the soliton output is shifted by approximately 100 nm with respect to the input spectrum of the pump field (Fig. 11a).

Propagation of laser radiation along the PCF is accompanied by third-harmonic generation giving rise to intense isolated peaks in the wavelength range of 380 – 550 nm (Fig. 11b). The central frequencies of these peaks agree very well with the frequencies where the effective mode index $n_{\rm sol}(\omega)$ of the soliton (the bold solid line in Fig. 11b) is matched with the mode index of one of the waveguide modes at the frequency 3ω (the fine solid lines in Fig. 11b). The phase-matching condition (25) is represented by the crossing of the $n_{\rm sol}(\lambda)$ dependence with the $n_m(\lambda/3)$ profile for one of the waveguide modes. The spectrum of the third-harmonic PCF output can be tuned by varying parameters of the input pump pulse. Thus, PCFs with appropriate dispersion profiles, providing efficient THG in the field of a soliton pump, can substantially enhance the abilities of femtosecond laser sources of infrared radiation by extending their operation range to the short-wavelength region, allowing efficient initiation and time-resolved studies of a broad class of photochemical and photobiological processes.

6. Nonlinear-optical transformation of nanosecond laser pulses and controlled supercontinuum generation in photonic-crystal fibers

The spatial, temporal, and spectral dynamics of the light field in a PCF depend on the properties of the fiber and the parameters of the input pulse. For pico- and nanosecond pulses [124 – 126], as well as for continuous-wave laser radiation [127, 128], the field evolution is dominated by stimulated Raman scattering (SRS) and four-wave mixing (FWM). In the case of femtosecond laser pulses, along with SRS and FWM, self- and cross-phase modulation, as well as soliton effects [31, 129, 130], play an important role in pulse dynamics. In this section, we discuss specific features of supercontinuum generation in PCFs, related to a strong parametric coupling between the Stokes and anti-Stokes SRS components of nanosecond pump pulses. The results of experiments presented below demonstrate efficient spectral transformation of nanosecond laser pulses in PCFs through parametric FWM and SRS. The experimental approach involves using a frequency-tunable laser source allowing various scenarios of laser-pulse transformation to be studied as a function of the pump frequency. The use of a tunable laser helps to identify regimes providing the maximum efficiency of supercontinuum transformation of nanosecond laser pulses. The results presented below in this section suggest that a strong parametric coupling between the Stokes and anti-Stokes SRS sidebands, occurring around the zero-GVD wavelength, can substantially increase the bandwidth and improve the spectral quality of supercontinuum radiation.

6.1 Phase matching for four-wave mixing in micro- and nanofibers

6.1.1 Four-wave mixing. Four-wave mixing in a nonlinear optical fiber involves a parametric decay of a laser field with a frequency $\omega_{\rm p}$ into sidebands through the process $2\omega_{\rm p} = \omega_{\rm a} + \omega_{\rm s}$, transferring some fraction of the energy from the pump field with the frequency $\omega_{\rm p}$ to the Stokes and anti-Stokes sidebands centered at the frequencies $\omega_{\rm s}$ and $\omega_{\rm a}$, respectively. The efficiency of such an FWM process becomes especially high when the phase-matching condition

$$\Delta\beta = \beta_{\rm a} + \beta_{\rm s} - 2\beta_{\rm p} \qquad (26)$$

is satisfied, with $\beta_{\rm p}$, $\beta_{\rm s}$, and $\beta_{\rm a}$ being the propagation constants of the pump, Stokes, and anti-Stokes fields in the guided modes of the waveguide structure considered. The nonlinear additive to the refractive index of the fiber material, induced by an intense pump field, changes the propagation constants of the waveguide modes [2]. The phase-matching condition (26) then becomes dependent on the peak power P of the pump field.

Let us represent the propagation constants β_s and β_a as power series about the central pump frequency ω_p:

$$\beta_s \approx 2\gamma P + \beta_p - \left(\frac{\partial\beta}{\partial\omega}\right)_{\omega_p}\Omega + \left(\frac{\partial^2\beta}{\partial\omega^2}\right)_{\omega_p}\frac{\Omega^2}{2} - \left(\frac{\partial^3\beta}{\partial\omega^3}\right)_{\omega_p}\frac{\Omega^3}{6} + \left(\frac{\partial^4\beta}{\partial\omega^4}\right)_{\omega_p}\frac{\Omega^4}{24} + \ldots, \qquad (27)$$

$$\beta_a \approx 2\gamma P + \beta_p + \left(\frac{\partial\beta}{\partial\omega}\right)_{\omega_p}\Omega + \left(\frac{\partial^2\beta}{\partial\omega^2}\right)_{\omega_p}\frac{\Omega^2}{2} + \left(\frac{\partial^3\beta}{\partial\omega^3}\right)_{\omega_p}\frac{\Omega^3}{6} + \left(\frac{\partial^4\beta}{\partial\omega^4}\right)_{\omega_p}\frac{\Omega^4}{24} + \ldots, \qquad (28)$$

where $\Omega = \omega_a - \omega_p = \omega_p - \omega_s$, $\gamma = 2\pi n_2 (\lambda S)^{-1}$ is the nonlinearity coefficient of the fiber, n_2 is the nonlinear refractive index of the fiber material, λ is the radiation wavelength, and S is the effective mode area.

We can now use expressions (27) and (28) to represent the phase-matching condition (26) as

$$\Delta\beta \approx 2\gamma P + \left(\frac{\partial^2\beta}{\partial\omega^2}\right)_{\omega_p}\Omega^2 + \left(\frac{\partial^4\beta}{\partial\omega^4}\right)_{\omega_p}\frac{\Omega^4}{12} + \ldots . \qquad (29)$$

In a widely employed approximation $(\partial^k\beta/\partial\omega^k)_{\omega_p} = 0$ for $k > 3$ [38], the solution to Eqn (29) for the frequency offset Ω providing phase matching for the FWM process is written in the following form:

$$\Omega \approx \left(\frac{2\gamma P}{|\beta_2|}\right)^{1/2}, \qquad (30)$$

where $\beta_2 = (\partial^2\beta/\partial\omega^2)_{\omega_p}$ is the second-order dispersion coefficient controlling the GVD of the waveguide mode at the pump frequency. With $(\partial^k\beta/\partial\omega^k)_{\omega_p} = 0$ for $k > 3$, the FWM phase-matching condition can be satisfied, as is seen from Eqns (29) and (30), if the parameter β_2 is negative and small in its absolute value, implying that the pump radiation wavelength should lie within the region of anomalous dispersion of the waveguide mode around the zero-GVD point.

Generally, dispersion profiles of waveguide modes in PCFs are quite complicated and cannot be described by including only the terms that are liner, quadratic, and cubic in Ω in series expansions (27) and (28). For a more accurate analysis, we examine below the propagation-constant mismatch $\Delta\beta$ calculated from the exact PCF dispersion curves for the $2\omega_p = \omega_a + \omega_s$ FWM process with the pump field centered at $\lambda_p = 598$ nm.

As a model of a waveguide structure with a small mode area, providing a high optical nonlinearity, we consider a cylindrical rod with a radius a made of a transparent dielectric material with a refractive index n_1, surrounded by a transparent dielectric material with a refractive index n_2. We further assume that the waveguide has a silica core (with n_1 calculated using the Sellmeyer equation for fused silica [2]) and an air cladding. Figure 12a presents the wavelength dependences of the parameter $\Delta\beta$ for a waveguide with a core radius $a = 627$ nm in the regime of weak pump ($P = 0$)

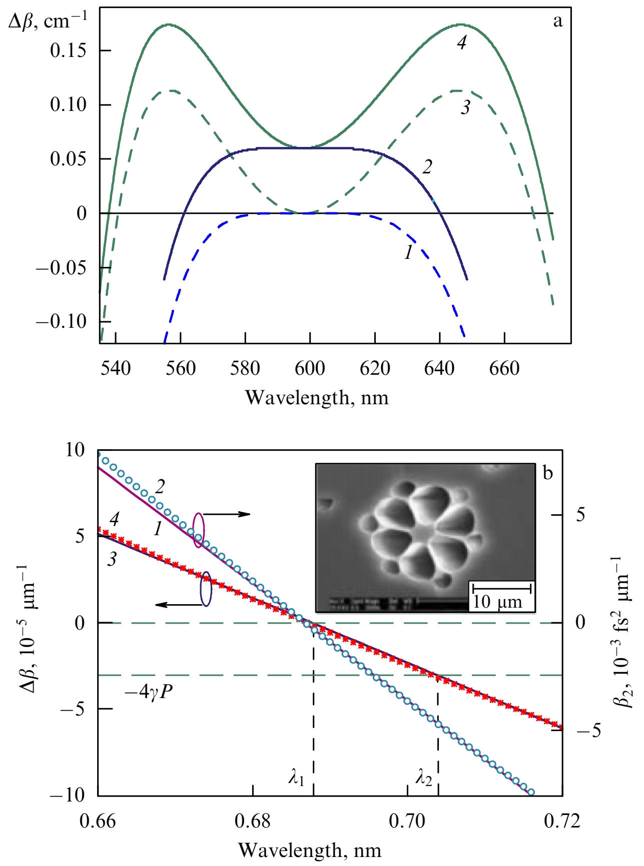

Figure 12. (a) Propagation-constant mismatch $\Delta\beta$ as a function of radiation wavelength for the $2\omega_p = \omega_a + \omega_s$ parametric FWM process in a microchannel waveguide with a core radius of 627 nm (*1*, *2*) and 630 nm (*3*, *4*). The pump wavelength is 598 nm. The γP parameter is set equal to 0 (*1*, *3*) and 6 m^{-1} (*2*, *4*). (b) Dispersion properties and FWM phase mismatch for an off-center microchannel waveguide in a silica PCF with a radius $a \approx 0.9$ μm: (*1*) dispersion parameter β_2 as a function of the pump wavelength, (*2*) approximation of the wavelength dependence of β_2 with Eqn (42), (*3*) propagation-constant mismatch $\Delta\beta_R$ for the $2\omega_p = \omega_a + \omega_s$ FWM process with $\omega_s = \omega_p - \Omega_R$ and $\omega_a = \omega_p + \Omega_R$, and (*4*) approximation of $\Delta\beta_R$ with Eqn (43). The dashed horizontal lines show the boundaries of the $0 > \Delta\beta_R > -4\gamma P$ region for $P = 80$ W. The inset shows an SEM cross-section image of the photonic-crystal fiber.

and with a pump power corresponding to $\gamma P = 6$ m^{-1}. As can be seen from the results presented in this figure, an increase in the peak power of the pump field substantially changes phase matching for the FWM process considered.

Dispersion profiles of waveguide structures with small core areas are highly sensitive to small variations in lateral dimensions of the core. In particular, for a waveguide with a core radius $a = 627$ nm, phase matching for the considered FWM process with $\gamma P = 6$ m^{-1} is achieved, as can be seen from Fig. 12a, for the Stokes and anti-Stokes wavelengths $\lambda_s \approx 641$ nm and $\lambda_a \approx 560$ nm. With the same value of the γP parameter, a waveguide with a core radius $a = 630$ nm provides phase matching for $\lambda_s \approx 538$ nm and $\lambda_a \approx 673$ nm.

6.1.2 Stimulated Raman scattering. Stimulated Raman scattering of narrowband laser radiation, including nano- and picosecond laser pulses, in silica waveguides gives rise to the generation of the Stokes radiation component separated from the frequency of the pump field by the frequency of Raman-active phonon vibrations of silica, $\Omega_R \approx 440$ cm^{-1} [2]. In certain spectral regions, a parametric FWM process $2\omega_p = \omega_a + \omega_s$ provides a strong coupling between this Stokes SRS component and the anti-Stokes field at the frequency $\omega_a = \omega_p + \Omega_R$. According to the general theory of SRS [105, 131], such a strong coupling between the Stokes and anti-Stokes SRS components may occur within two frequency ranges lying on either side of the frequency where the phase matching condition (26) is satisfied for the pump field and its Stokes and anti-Stokes sidebands. Under the assumption $(\partial^k \beta/\partial\omega^k)_{\omega_p} = 0$ for $k > 3$, the propagation-constant mismatch for the pump, Stokes, and anti-Stokes fields involved in the FWM process can be written as follows:

$$\Delta\beta_R \approx \beta_2(\omega_p)\,\Omega_R^2\,. \tag{31}$$

An important difference of SRS in optical fibers from the textbook regimes of SRS occurring in gas-phase media is associated with a considerable asymmetry of the frequency profile of the gain for the Stokes and anti-Stokes SRS components with respect to the frequency whereat the condition $\Delta\beta_R = 0$ is satisfied. To demonstrate this property of SRS in optical fibers, we follow the analysis of Shen and Bloembergen [105, 131] and represent the slowly varying amplitudes of the Stokes and anti-Stokes SRS components as

$$E_s = \left[A_s \exp(\mathrm{i}\Delta K_+ z) + B_s \exp(\mathrm{i}\Delta K_- z)\right] \exp\left[(\mathrm{i}\beta_s - \alpha_s) z\right], \tag{32}$$

$$E_a^* = \left[A_a^* \exp(\mathrm{i}\Delta K_+ z) + B_a^* \exp(\mathrm{i}\Delta K_- z)\right] \times \exp\left[(-\mathrm{i}\beta_a + \mathrm{i}\Delta\beta_R - \alpha_a) z\right], \tag{33}$$

where

$$\Delta K_\pm = \pm\left[\left(\frac{\Delta\beta_R}{2}\right)^2 + \Delta\beta_R Q\right]^{1/2} - \frac{\Delta\beta_R}{2}\,, \tag{34}$$

$$Q = \frac{2\pi\omega_s^2}{c^2\beta_s}\,\chi^{(3)}|E_p|^2\,, \tag{35}$$

$\chi^{(3)}$ is the third-order nonlinear-optical susceptibility of the fiber material, and E_p is the amplitude of the pump field.

For large phase mismatches, $|\Delta\beta_R| \gg |Q|$, there is no coupling between the Stokes and anti-Stokes SRS components. The anti-Stokes field then rapidly decays, while the Stokes component experiences amplification in the standard SRS regime with the gain $G_R = 2\,\mathrm{Im}\,\Delta K_-$. On exact phase matching, $\Delta\beta_R = 0$, the coupling between the Stokes and anti-Stokes components reaches its maximum. However, no exponential gain is observed for any of the SRS components in this regime. These two important SRS regimes have been analyzed in the classical texts on nonlinear optics [105, 131].

Of primary interest for us here is the regime of SRS with a small, but nonzero, phase mismatch, $|\Delta\beta_R| \ll |Q|$. In this case, Eqn (34) yields

$$\Delta K_\pm \approx \pm(\Delta\beta_R Q)^{1/2}\,. \tag{36}$$

For $\Delta\beta_R > 0$, the gain for the Stokes and anti-Stokes components, as can be seen from Eqns (32) and (33), is then given by

$$G_1\left(|\Delta\beta_R|\right) \approx \left(|\Delta\beta_R|\,\rho\right)^{1/2} \sin\frac{\varepsilon}{2}\,, \tag{37}$$

where the amplitude $\rho = \left[(\mathrm{Re}\,Q)^2 + (\mathrm{Im}\,Q)^2\right]^{1/2}$ and the argument $\tan\varepsilon = \mathrm{Im}\,Q/\mathrm{Re}\,Q$ of the complex parameter Q were introduced.

For $\Delta\beta_R < 0$, the gain of the Stokes and anti-Stokes fields is equal to

$$G_2\left(|\Delta\beta_R|\right) \approx \left(|\Delta\beta_R|\,\rho\right)^{1/2} \cos\frac{\varepsilon}{2}\,. \tag{38}$$

The ratio

$$\frac{G_2}{G_1} \approx \cot\frac{\varepsilon}{2} \tag{39}$$

quantifies the asymmetry of the frequency profile of the SRS gain with respect to the frequency where $\Delta\beta_R = 0$.

For an important particular case of a strong Raman resonance (e.g., in the gas phase), we derive the following relations for the spectral region where the maximum SRS gain is achieved:

$$\left|\mathrm{Im}\,Q\right| \propto \left|\chi_R^{(3)}\right| \gg \left|\mathrm{Re}\,Q\right| \propto \left|\chi_{nr}^{(3)}\right|,$$

where $\left|\chi_R^{(3)}\right|$ and $\left|\chi_{nr}^{(3)}\right|$ are the resonant and nonresonant parts of the third-order nonlinear-optical susceptibility. In this regime, we find that

$$\varepsilon \approx \frac{\pi}{2} - \frac{\mathrm{Re}\,Q}{\mathrm{Im}\,Q}\,,$$

and formula (39) gives the following result:

$$\frac{G_2}{G_1} \approx 1 + \frac{\mathrm{Re}\,Q}{\mathrm{Im}\,Q}\,.$$

The slight asymmetry of the frequency profile of the SRS gain relative to the frequency where $\Delta\beta_R = 0$ in this case is due to the nonresonant part of the nonlinear-optical susceptibility.

For silica fibers, the situation is somewhat opposite, as now the Raman part of the nonlinear-optical susceptibility can be considered as a correction (18%) to the electronic part (82%) in the overall nonlinear-optical response of the material. Using a standard Lorentzian-line model for the SRS gain profile, we represent the real and imaginary parts of the Q parameter as

$$\mathrm{Re}\,Q = Q_{nr} + \frac{Q_R}{1 + \Omega^2/\Omega_0^2}\,, \tag{40}$$

$$\mathrm{Im}\,Q = \frac{\Omega}{\Omega_0}\,\frac{Q_R}{1 + \Omega^2/\Omega_0^2}\,, \tag{41}$$

where Ω is the frequency detuning from the center of the SRS gain profile, Ω_0 is the linewidth, Q_R is the amplitude of the Raman resonance response, and Q_{nr} is the real parameter characterizing the nonresonant (electronic) part of the nonlinear-optical susceptibility.

With $\Omega = \Omega_0$, Eqns (40) and (41) yield $G_2/G_1 \approx 4Q_{nr}/Q_R$. Since the electronic part of the nonlinear-optical response of fused silica is substantially larger than the Raman part of this response, the gain of the Stokes and anti-Stokes components in the region where $\Delta\beta_R < 0$ should be appreciably higher than the SRS gain in the region where $\Delta\beta_R > 0$.

Calculated results presented in Fig. 12b define the regions of strong FWM coupling of the Stokes and anti-Stokes components resulting from the SRS process in an off-center microchannel waveguide in a microstructured cladding of a silica fiber with the cross-section structure shown in the inset to this figure. The radius of the microchannel waveguide is 0.9 μm. The solid line *1* in Fig. 12b presents the parameter β_2 for such a waveguide as a function of the pump wavelength. Around the zero-GVD frequency ω_0, the parameter β_2 can be approximated (line *2* in Fig. 12b) by the formula

$$\beta_2(\omega_p) \approx \beta_3(\omega_0)\,\delta\omega\,, \tag{42}$$

where $\beta_3 = \partial^3\beta/\partial\omega^3$, and $\delta\omega = \omega_p - \omega_0$.

The mismatch of the propagation constants of the pump field and SRS components involved in the FWM process can then be represented as

$$\Delta\beta_R \approx \beta_3(\omega_0)\,\Omega_R^2\delta\omega\,. \tag{43}$$

To assess the accuracy of this approximation, the phase mismatch calculated with the use of Eqn (43) was compared with the parameter $\Delta\beta_R$ calculated as a function of the pump wavelength, for the exact dispersion profile of the considered waveguide, determined by means of numerical simulations (line *3* in Fig. 12b). This comparison shows (see Fig. 12b) that, within a limited spectral interval, the error in the approximation provided by Eqn (43) does not exceed several percent.

We can now combine expression (43) and the condition of strong coupling of the Stokes and anti-Stokes SRS components, viz.

$$0 > \Delta\beta_R > -4\gamma P\,, \tag{44}$$

to derive the following explicit formula for the band $\Delta\omega_R$ of pump frequencies, where the pump field is phase-matched with the Stokes and anti-Stokes SRS components:

$$|\Delta\omega_R| \approx 4\gamma P\left[\beta_3(\omega_0)\right]^{-1}\Omega_R^{-2}\,. \tag{45}$$

The vertical dashed lines in Fig. 12b represent the boundaries of the spectral region ($\lambda_1 \approx 688$ nm, $\lambda_2 \approx 704$ nm) where the FWM process considered is phase-matched, giving rise to a strong coupling between the Stokes and anti-Stokes SRS components of the light field in the waveguide. Theoretical predictions for the wavelengths λ_1 and λ_2, corresponding to the boundaries of the spectral region where the Stokes and anti-Stokes components are strongly coupled to each other, agree well with the results of experiments presented below in this paper. Efficient generation of anti-Stokes SRS components in the spectral band $\Delta\omega_R$ enhances the high-frequency tail of the radiation spectrum at the output of the fiber, thus increasing the bandwidth and improving the spectral quality of supercontinuum radiation in the regime of high peak powers of the pump field.

6.2 Nonlinear-optical transformation of nanosecond laser pulses in photonic-crystal fibers

Experiments [132] were devoted to the investigation of nonlinear-optical processes in off-center microchannel waveguides with a diameter ranging from 0.5 to 2.0 μm in the nodes of the microstructured cladding (see the inset to Fig. 12b) of silica fibers. These fibers were fabricated [133–135] by drawing from a preform consisting of an array of silica capillaries and a solid silica rod at the center of the structure. The fiber length was varied in nonlinear-optical experiments from 20 to 150 cm, depending on the size of the microchannel waveguide and the magnitude of optical loss.

A wavelength-tunable dye laser served as a source of input laser radiation. This laser was pumped by the second-harmonic output of a *Q*-switched Nd:YAG laser. Second-harmonic pulses used to pump the dye laser had a central wavelength of 532 nm, a pulse width of about 10 ns, and an energy of about 5 mJ. With such parameters of pump radiation, a standard set of dyes enabled the generation of tunable radiation at the output of the dye laser within the range of wavelengths from 545 to 710 nm. The broad range of wavelength tunability provided by the dye laser helped to determine the regions of maximum FWM and SRS light-pulse transformation efficiency for a broad variety of microchannel waveguides with different shapes and lateral dimensions.

For the excitation of guided modes of PCF microchannel waveguides (Fig. 13), dye-laser radiation was tightly focused on the input end of a fiber, which was aligned with the laser beam in such a way as to provide the maximum spatial overlap of the laser beam and a microchannel waveguide in the transverse plane. The spectrum of radiation at the output of the fiber was measured with the use of an OceanOptics® spectrum analyzer. The ranges of parameters providing efficient FWM transformation of laser pulses were identified by scanning the frequency of dye-laser radiation.

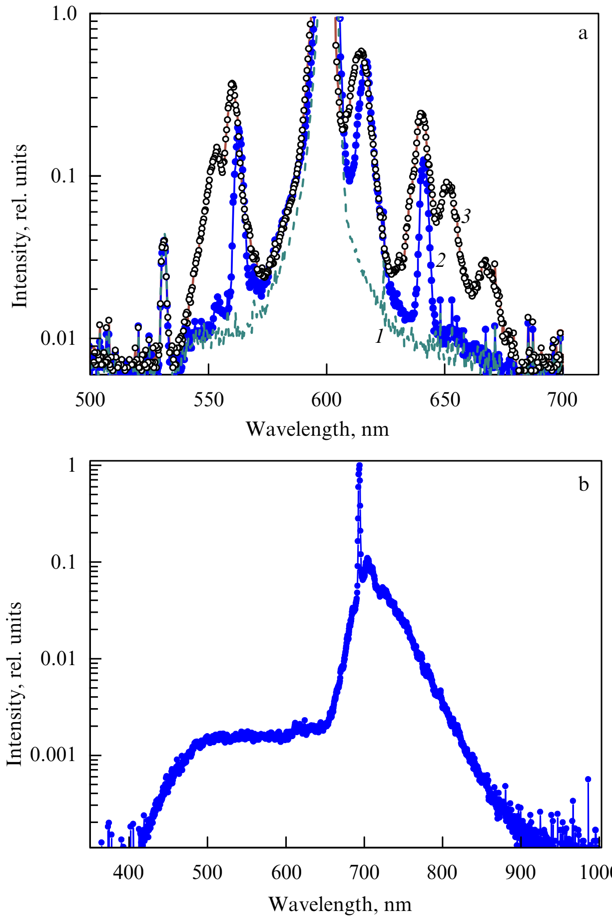

Figure 13. (a) Radiation spectra detected at the output of a PCF microchannel waveguide with a diameter of 0.63 μm and a length of 85 cm. The pump pulses have an input pulse width of 15 ns, a central wavelength of 598 nm, and a peak power of about 1 W (dashed line *1*), 40 W (line *2*), and 80 W (line *3*). (b) Generation of broadband radiation in a 100-cm silica PCF microchannel waveguide off the strong Stokes–anti-Stokes coupling region with $\gamma P \approx 10$ m^{-1}.

Figure 13a displays typical radiation spectra recorded at the output of a microchannel waveguide with a core radius of about 630 nm. In accordance with the calculated results shown in Fig. 12a (see Section 6.1.1), the pump wavelength in these experiments was varied from 590 to 610 nm. As can be seen from the experimental results presented in Fig. 13a, efficient FWM conversion of nanosecond laser pulses is achieved with the pump wavelength $\lambda_p \approx 598$ nm. In accordance with the results of numerical analysis for the off-center microchannel waveguides in a PCF with the cross-section structure shown in the inset to Fig. 12b, the nonlinearity coefficient for silica microfibers with a characteristic core radius $a \approx 0.63$ μm at the wavelength of 600 nm is $\gamma \approx 150$ W^{-1} km^{-1}. Thus, the optical nonlinearity of the studied type of waveguide structures is an order of magnitude higher than the typical nonlinearity of standard fibers.

Curve *1* in Fig. 13a shows the radiation spectrum detected at the output of the microchannel waveguide in a PCF with a length $L \approx 85$ cm. The pump radiation in these experiments had a wavelength $\lambda_p \approx 598$ nm and a peak power of about 1 W. The length of nonlinear interaction, $l_{nl} = (\gamma P)^{-1}$, for laser pulses with such a peak power is about 7 m. Since this nonlinear length is much larger than the fiber length chosen for experiments, the spectrum of the fiber output is nearly identical to the spectrum of the input laser field.

As the peak power of the pump pulse increases, intense sidebands show up in the spectrum of the fiber output (curves *2* and *3* in Fig. 13a). With a peak power of the pump pulse $P \approx 40$ W ($l_{nl} \approx 17$ cm), the Stokes and anti-Stokes sidebands in the fiber output spectrum are centered at the wavelengths $\lambda_s \approx 641$ nm and $\lambda_a \approx 560$ nm (curve *2* in Fig. 13a), which agrees well with the analysis of phase matching for the $2\omega_p = \omega_a + \omega_s$ FWM process (cf. Figs 12a and 13a). A further growth in the pump power leads to the broadening of the Stokes and anti-Stokes sidebands (curve *3* in Fig. 13a), which eventually yields a fiber output with a broad continuous spectrum.

An intense peak centered at approximately 614 nm in the spectra presented in Fig. 13a corresponds to the Stokes SRS component. Generation of its anti-Stokes counterpart is suppressed for a microfiber with a core radius $a \approx 0.63$ μm, because the relevant FWM process is phase-mismatched and cannot efficiently couple the Stokes and anti-Stokes sidebands. As can be seen from Figs 12a and 13, phase-matching conditions are satisfied in these experiments for frequency offset values of Ω considerably exceeding Ω_R.

Theoretical analysis, as outlined in Section 6.1.2, predicts a strong coupling of Stokes and anti-Stokes SRS sidebands for a silica PCF microchannel waveguide (see the inset to Fig. 12b) with a core radius $a \approx 0.9$ μm. With the pump wavelength ranging from 690 to 705 nm, intense Stokes and anti-Stokes sidebands of the first and higher orders are observed in the spectrum of radiation at the output of such a fiber (see Fig. 14). When the peak power of the pump field becomes sufficiently high, self- and cross-phase modulation, as well as cascade FWM processes, broaden the Stokes and anti-Stokes SRS components. Under these conditions, radiation with a broad continuous spectrum (white light, or a supercontinuum) is observed at the output of the fiber. A strong parametric coupling between Stokes and anti-Stokes SRS components, provided by the phase-matched FWM of the pump field and its Stokes and anti-Stokes sidebands, helps to considerably increase the spectral content and to improve the spectral quality of supercontinuum radiation. This effect is illustrated by the experimental results presented in Figs 13 – 15. When FWM is phase-mismatched, failing to efficiently couple the Stokes and anti-Stokes SRS components, the nonlinear-optical transformation of the pump field in a microfiber yields a radiation with a spectral content confined to the range of wavelengths from 680 to 730 nm.

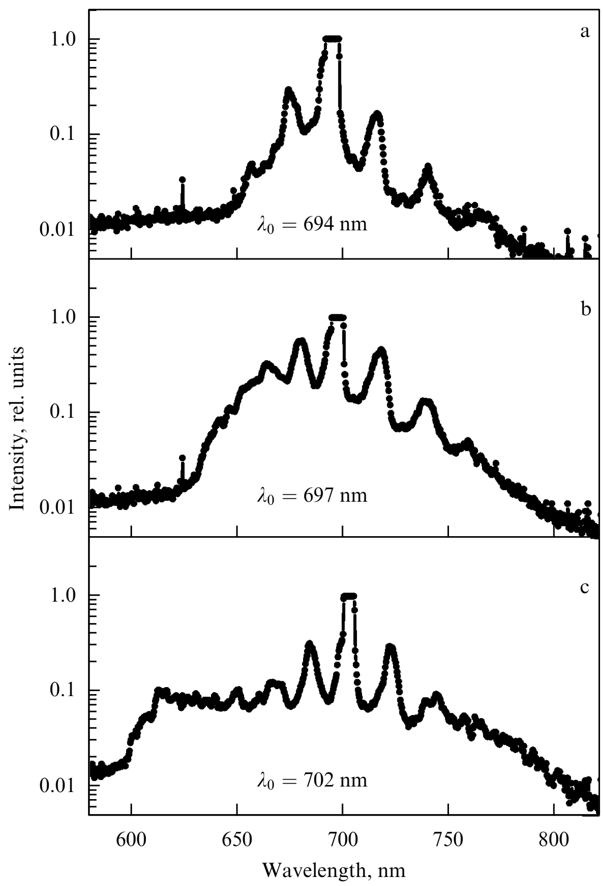

Figure 14. Radiation spectra measured at the output of the PCF microchannel waveguide with a diameter of 0.9 μm and a length of 85 cm. The input pump pulse has a peak power of 80 W and a central wavelength of 694 nm (a), 697 nm (b), and 702 nm (c).

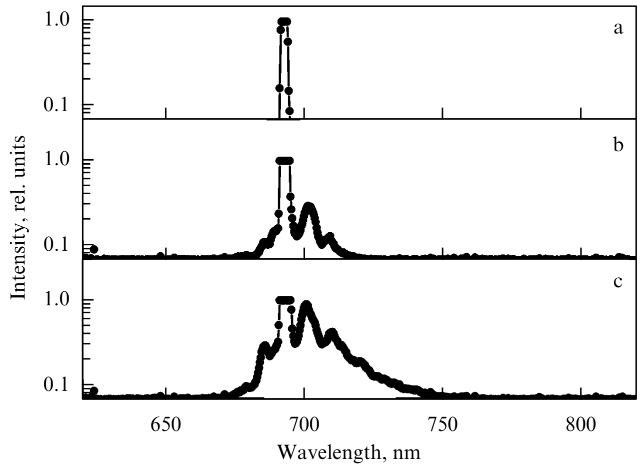

Figure 15. Generation of broadband radiation by nanosecond laser pulses in microchannel waveguides with different diameters in an 85-cm silica PCF off the strong Stokes – anti-Stokes coupling region with $\gamma P \approx 0.2$ m^{-1} (a), 3.5 m^{-1} (b), and 7.5 m^{-1} (c).

Even for high peak powers of the pump field, the intensity of the high-frequency wing in the output radiation spectrum is much lower than the intensity of the Stokes part of this spectrum (Fig. 13b).

A strong coupling between the Stokes and anti-Stokes components substantially enhances the high-frequency wing of the output spectrum, thus considerably enriching the spectral content of supercontinuum radiation. The fiber output spectra shown in Figs 14c and 15c were taken at the same value of the nonlinear interaction length, $\gamma P \approx 7.5\ \mathrm{m}^{-1}$. However, since, in the case of experiments presented in Fig. 14c, the pump wavelength is chosen in such a way as to allow a phase-matched parametric FWM coupling of the SRS sidebands, the fiber output spectrum in Fig. 14c is much broader, stretching from 610 to 760 nm.

7. Generation of intense supercontinuum radiation in large-mode-area photonic-crystal fibers

The high efficiency of nonlinear-optical interactions in PCFs is due to the strong confinement of electromagnetic radiation in a small, micrometer-sized fiber core [11, 29]. In a special class of highly nonlinear PCFs designed for efficient supercontinuum generation and frequency conversion of ultrashort laser pulses [136–144], a small core with a diameter on the order of or less than a micron provides high power densities even for low-energy (nanojoule and subnanojoule) ultrashort light pulses, leading to ultimate efficiencies of nonlinear-optical interactions. Small-core PCFs also allow dispersion [25, 26] and birefringence [145] tailoring through fiber structure engineering. Designing optical fibers for the nonlinear-optical transformation of high-peak-power laser pulses is much more complicated. Laser pulses with pulse widths on the order of hundreds of femtoseconds with fluences of several joules per square centimeter induce an optical breakdown in the bulk of fiber material [146]. Fibers with large core diameters, on the other hand, do not offer much flexibility in dispersion engineering. In particular, silica large-core fibers cannot provide anomalous dispersion for Ti:sapphire-laser radiation (with a central wavelength of 800 nm), thus excluding realization of attractive soliton regimes of nonlinear-optical interactions of such pulses, limiting the efficiency of supercontinuum generation and frequency conversion for ultrashort light pulses delivered by this class of laser sources.

In experiments [64, 65, 147], high-power supercontinuum generation was demonstrated using large-mode-area (LMA) PCFs [57, 58] and a femtosecond Cr:forsterite laser [148] as a pump source. In the initial stage of laser-pulse dynamics in the fiber, the spectral broadening of femtosecond laser pulses gives rise to sidebands some of which fall within the region of anomalous dispersion. These frequency components undergo soliton spectral–temporal transformation processes, leading to an efficient supercontinuum generation in the near-IR range with an energy exceeding 1 μJ.

The fibers used in experiments [64, 147] were fabricated by the stack-and-draw technology. A preform consisted of silica capillary tubes with a solid silica rod at the center of the structure. For highly efficient supercontinuum transformation of high-peak-power femtosecond laser pulses, a family of PCFs with a hexagonal lattice of air holes in the fiber cladding (see the inset to Fig. 16) with different diameters of air holes d and lattice pitches Λ was fabricated. The best performance was achieved for PCFs with $d/\Lambda \approx 0.36$ and a core diameter

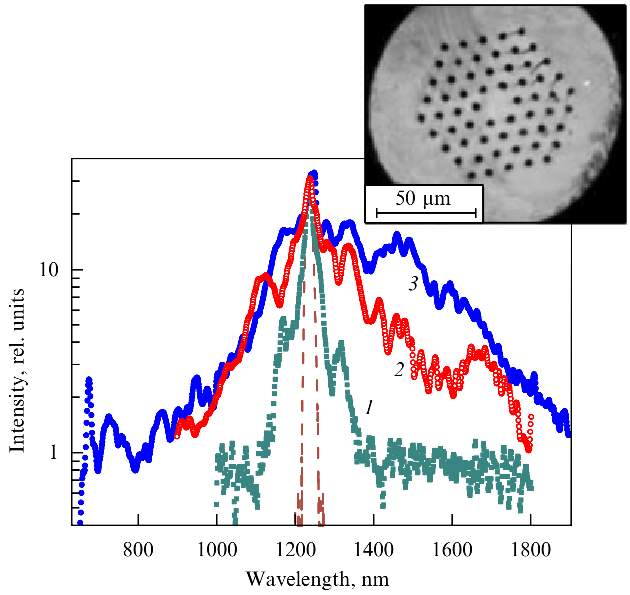

Figure 16. Spectra of laser radiation transmitted through a PCF with an effective mode area of 380 μm^2 and a length of 20 cm. The initial pulse width is 300 fs. The input laser pulse energy is (*1*) 0.15 μJ, (*2*) 0.98 μJ, and (*3*) 1.3 μJ. The dashed line illustrates the spectrum of the input laser pulse. The inset presents a cross-section image of a large-mode-area photonic-crystal fiber.

of about 22 μm. The fundamental guided mode in such a fiber has an effective area of about 380 μm^2. Photonic-crystal fibers with such a d/Λ ratio are multimode. However, the number of modes supported by such fibers is much less than the number of modes in a fiber with the same core diameter and a solid cladding. The mismatch of the propagation constants for the adjacent modes in such a PCF is much larger than the mismatch of propagation constants in a fiber with a solid cladding, which stabilizes waveguide modes with respect to nonlinear-optical cross-talk with other modes.

The laser system used in experiments [64, 147] consisted of a Cr^{4+}:forsterite master oscillator pumped with an ytterbium fiber laser, a stretcher, an optical decoupler, a regenerative amplifier, a compressor, and a frequency-doubling nonlinear crystal. The master oscillator delivered 30–60-fs pulses at a repetition rate of 120 MHz [148] at a central frequency of 1250 nm with an average power of about 180 mW. These laser pulses were stretched in order to be amplified in an Nd:YLF-laser-pumped regenerative amplifier up to about 100 μJ. The amplified light pulses were recompressed to a minimum pulse width of 90 fs by a grating compressor. In the experiments reported here, the compressor was adjusted in such a way as to provide linearly chirped light pulses stretched up to 300 fs in order to reduce or avoid effects related to the self-focusing of high-peak-power laser pulses in the fiber, including laser damage to the fiber.

Figure 16 displays typical spectra of radiation detected at the output of an LMA PCF with a core diameter of 22 μm and a length of 20 cm for different energies of input laser pulses. For low energies of input laser pulses, the output spectra feature Stokes and anti-Stokes sidebands (curve *1* in Fig. 16) lying in the regions of anomalous and normal dispersion, respectively. Generation of these sidebands indicates the significant role of parametric four-wave mixing giving rise to frequency-shifted spectral components originating from the modulation instability of the pump field (the laser pulse). This process is automatically phase-matched when the central wavelength of the pump field is close to the wavelength of zero group-velocity dispersion [2]. This condition, which is of key importance for highly efficient frequency conversion, was satisfied in the experiments considered.

As the energy of the input laser pulse increases, the Stokes and anti-Stokes sidebands undergo spectral broadening, eventually forming a broadband spectrum at the output of the fiber. For input laser pulses with an initial energy of about 1.30 μJ, the spectrum of the broadband signal at the output of a 20-cm PCF, as can be seen from the experimental data presented in Fig. 16, stretches from 700 to 1800 nm. The total energy of this signal was estimated as 1.15 μJ.

The powerful low-frequency wing of the output spectrum in this regime (curve *3* in Fig. 16) suggests the importance of soliton mechanisms of nonlinear-optical transformation of laser pulses. This conclusion is also supported by studies of the spectral – temporal evolution of the laser field in the PCF, performed in experiments [64, 147] with the use of cross-correlation frequency-resolved optical gating (XFROG) [149, 150]. In XFROG, information on the spectral and temporal properties of the output light field, including its chirp and the spectral phase, is retrieved by measuring the intensity of the sum-frequency signal generated in an LBO crystal by the PCF output and the fundamental-wavelength pulse from the Cr: forsterite laser as a function of the delay time τ between these two pulses. Soliton phenomena are visualized in XFROG traces as a spiky structure of the temporal envelope of the pulse intensity. The chirp of the PCF output suggests no technically simple way of compressing the supercontinuum PCF output to a transform-limited ultrashort pulse corresponding to the full spectral width of this field. However, information on the phase of the PCF output provided by XFROG measurements can be employed for pulse compression through the compensation of a complex spectral phase of the PCF output with the use of a spatial light modulator. This strategy of pulse compression of PCF output had been earlier implemented in Refs [46, 151].

8. Hollow photonic-crystal fibers for the soliton delivery of megawatt femtosecond pulses

8.1 Hollow photonic-crystal fibers in the nonlinear optics of high-peak-power light pulses

Optical solitons are interesting physical objects that are intensely studied in optical science and that offer attractive methods for large-distance transmission of optical signals and allow observation of new nonlinear-optical effects [152, 153]. Optical fibers enable the formation of solitons characterized by a stable or slowly evolving envelope within characteristic propagation lengths from several centimeters to kilometers [2]. The power and energy of solitons in optical fibers is limited by the laser-damage threshold of optical materials, as well as by factors inherent in the nature of optical solitons. Formation of an isolated fundamental soliton becomes possible through a precise balance between dispersion and optical nonlinearity. The peak power P of a laser pulse that provides such a balance can be found by equating the nonlinear interaction length $L_{\mathrm{nl}} = (\gamma P)^{-1}$ (where γ is the nonlinearity coefficient) and the dispersion length $L_{\mathrm{d}} = \tau_0^2/|\beta_2|$ (where τ_0 is the soliton pulse width, $\beta_2 = \partial^2\beta/\partial\omega^2$, β is the propagation constant of the waveguide mode, and ω is the radiation frequency). The maximum power of the fundamental soliton is thus given by $P_{\mathrm{s}} = |\beta_2|\gamma^{-1}\tau_0^{-2}$. For typical nonlinearity and dispersion parameters of a standard silica optical fiber, $\gamma \sim 10\ \mathrm{W}^{-1}\,\mathrm{km}^{-1}$ and $|\beta_2| \sim 10\ \mathrm{ps}^2\,\mathrm{km}^{-1}$, the fundamental soliton with a pulse width of 100 fs has a typical peak power of 100 W. The increase in the power of laser radiation leads to the generation of higher-order solitons with a more complicated spectral and temporal field structure and pulse-evolution dynamics [2].

Hollow waveguides offer attractive options for the delivery and nonlinear-optical spectral and temporal transformation of high-peak-power laser pulses [21]. The laser-breakdown threshold of a gas filling the core of such a waveguide is much higher than the breakdown threshold characteristic of a dielectric waveguide. However, standard, capillary type hollow waveguides with a solid dielectric cladding are intrinsically leaky [21], with the magnitude of optical loss scaling as λ^2/a^3 with a core radius a and radiation wavelength λ. Experiments with hollow fibers are, therefore, inevitably restricted to waveguides with large core diameters, which are essentially multimode [154].

Hollow-core PCFs [15 – 17] can support robust isolated truly guided modes of high-peak-power ultrashort light pulses and enable efficient nonlinear-optical transformations of such fields [155 – 160]. Since the optical nonlinearity of gas-phase media under normal conditions is three orders of magnitude lower (e.g., for atmospheric air) than the nonlinearity of fused silica, while the optical breakdown threshold of gases is much higher than the breakdown threshold of transparent dielectrics, gas-filled hollow PCFs can support soliton propagation regimes for femtosecond pulses with megawatt peak powers [161]. The soliton compression of high-peak-power ultrashort pulses is one of the interesting applications of soliton effects in hollow PCFs [162, 163]. High-peak-power solitons are interesting objects of optical physics, suggesting ways to develop novel fiber components for the transmission of high-power ultrashort light pulses and to create compact fiber-format systems for nonlinear micro-spectroscopy [164].

Hollow PCFs have been recently shown to allow the delivery of high-energy nano- and picosecond pulses for biomedical [165] and technological [166, 167] applications. These fibers also offer much promise for the creation of novel optical endoscopes [168, 169] and gas sensors [170]. In an optical endoscope demonstrated by Flusberg et al. [168], a hollow PCF provides a delivery of unamplified Ti:sapphire-laser pulses with a pulse width of 100 – 150 fs to an area of interest inside a living organism. The low nonlinearity of the gas filling the core of the fiber and the choice of the central wavelength of laser pulses close to the zero-GVD wavelength of the fiber helps to reduce temporal envelope distortions of the transmitted light signal.

In this section, we consider a radically different regime of ultrashort-pulse transmission through a hollow PCF. Soliton regimes of pulse propagation will be shown to suppress distortions of the temporal field envelope and allow the peak power of ultrashort laser pulses transmitted through a hollow fiber to be substantially increased. In experiments presented below, the second-harmonic output of a femtosecond Cr:forsterite-laser system with an amplification stage is employed as a source of input ultrashort light pulses. The peak power of solitons produced in these experiments is four orders of magnitude higher than the peak power of solitons attainable with standard optical fibers. Hollow PCFs allowing the transmission of megawatt femtosecond pulses without noticeable distortions of the temporal pulse envelope and energy loss suggest new attractive solutions for laser biomedicine and optical technologies.

8.2 Hollow photonic-crystal fibers and soliton delivery of high-peak-power femtosecond pulses

Hollow PCFs designed for the transmission of high-peak-power ultrashort laser pulses [164 – 166, 171] have the cross-section structure shown in inset 1 to Fig. 17. The diameter of the hollow core in these fibers is about 14 μm. The properties of waveguide modes in these structures were modelled by numerically solving the wave equation for the transverse components of the electric field through the expansion of the field and the refractive-index profile based on orthogonal polynomials. With such an expansion, the solution of the wave equation with the relevant boundary conditions is reduced to an eigenfunction and eigenvalue problem of a matrix equation for the expansion coefficients [172, 173]. The spectral and temporal dynamics of laser pulses were analyzed by numerically solving the generalized nonlinear Schrödinger equation [2] which included high-order dispersion, shock waves, and the retarded part of the optical nonlinearity of the gas filling the fiber core [174].

Numerical simulations performed for the considered type of hollow PCFs suggest that the second-harmonic pulses of the Cr:forsterite laser with an initial central wavelength of 618 nm can be transmitted through fibers in the soliton regime. For hollow PCFs filled with a Raman-active gas (atmospheric air in our experiments), the retarded part of optical nonlinearity has a significant influence on the temporal dynamics of an ultrashort light pulse propagating through the fiber. This part of the nonlinear response induces a continuous red shift of the soliton spectrum — a phenomenon that is well known in the dynamics of solitons in conventional optical fibers [2, 88, 89].

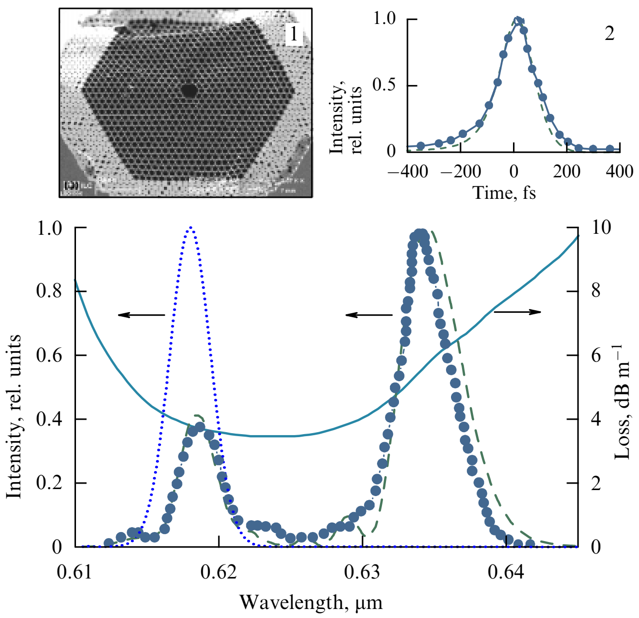

Figure 17. Intensity spectrum of a light pulse with an initial pulse width of 90 fs, an energy of 300 nJ, and a central wavelength of 618 nm transmitted through a hollow PCF filled with atmospheric air: dashed line — results of numerical simulations, circles — experimental data. The input spectrum of the laser field is shown by the dotted line. Also shown is the spectral dependence of waveguide loss. Inset 1 shows a cross-section image of the hollow PCF. Inset 2 presents the temporal envelope of the frequency-shifted soliton part of the PCF output: circles — reconstruction from XFROG measurements, dashed line — results of numerical simulations.

The dashed line in Fig. 17 presents the intensity spectrum calculated for a light pulse with an initial pulse width of 90 fs, energy of 300 nJ, and central wavelength of 618 nm transmitted through the considered type of hollow PCFs. The frequency-shifted soliton component of the output field is centered at the wavelength of 636 nm. In the time domain, the retarded nonlinearity and high-order dispersion effects split the light pulse propagating through the hollow PCF into two spectrally and temporally isolated features. The dashed line in inset 2 to Fig. 17 shows the temporal intensity envelope of the laser pulse, corresponding to the frequency-shifted soliton component of the PCF output. The typical pulse width of this soliton component is estimated as 120 fs. The spectral and temporal separation of the soliton component from the nonsolitonic part of the field increases as the radiation propagates along the fiber. This effect is related to the dispersion-induced difference in the group velocities of solitons with different local parameters, as well as the dependence of the soliton self-frequency shift on the local soliton pulse width.

The laser system used in experiments [164] consisted of a Cr^{4+}:forsterite master oscillator, a stretcher, an optical isolator, a regenerative amplifier, a compressor, and a crystal for frequency doubling. The spectrum of the laser pulse is shown by the dotted line in Fig. 17. The spectrum and the temporal envelope of the PCF output were recorded by using the XFROG technique [149, 150].

The measured intensity spectrum of the PCF output (the dots in Fig. 17) agrees well with the results of numerical simulations (the dashed line in Fig. 17). Most of the fiber output radiation energy is concentrated within the spectral peak corresponding to the frequency-shifted soliton. For input laser pulses with a pulse width of 90 fs, an energy of 300 nJ, and a central wavelength of 618 nm, the soliton part of the PCF output has the form of a 120-fs pulse with an energy of about 130 nJ (the dots in inset 2 to Fig. 17). The peak power of such a soliton reaches 1.1 MW.

As the input pulse energy increases, the soliton at the output of the PCF becomes shorter, which enhances the soliton self-frequency shift. This effect is readily observed in the measured spectra of PCF output, where the central wavelength of the output pulse becomes progressively longer as the input pulse energy increases. This finding is consistent with the basic properties of ideal solitons defined as solutions to the nonlinear Schrödinger equation. For these solitons, the peak power, as mentioned above, is related to the pulse width by the expression $P_s = |\beta_2|\gamma^{-1}\tau_0^{-2}$. The soliton self-frequency shift thus allows a continuous tuning of the central wavelength of the megawatt soliton PCF output through a variation of the input pulse energy.

8.3 Megawatt optical solitons in nonlinear microspectroscopy and laser biomedicine

Optical fibers supporting soliton regimes of propagation for megawatt femtosecond light pulses offer new attractive options for laser-beam delivery in optical technologies and laser biomedicine. A distortion-free transmission of high-peak-power femtosecond pulses can substantially enhance the capabilities of fiber-optic components designed for nonlinear microspectroscopy [164], laser endoscopy, and laser therapy and surgery using ultrashort laser pulses. In particular, PCFs designed for the transmission of unamplified femtosecond laser pulses with a typical energy of 0.1 – 1 nJ, a pulse width of 100 fs, and a repetition rate on the order of 100 MHz have been shown to be ideally suited for microendoscopy based on two-photon fluorescence [168, 169]. Microendoscopes based on photonic band-gap fibers with a solid [169] and a hollow [168] core have been recently demonstrated. On the other hand, regeneratively amplified femtosecond pulses provide a powerful tool for nanosurgery [175], laser ophthalmology [176, 177], vessel photodisruption [178], and optical histology [179]. A fiber-optic delivery of such pulses is usually accompanied by pulse distortions induced by nonlinear-optical phenomena. As shown above, hollow PCFs can resolve this difficulty. Fibers of this type show much promise for laser dentistry. Pico- and femtosecond laser pulses in the near-infrared range have been shown to allow the heat load on dental tissues to be radically reduced and microcracking to be avoided [180, 181]. Hollow PCFs allow a fiber-format delivery of high-energy nano- and picosecond laser pulses intended for the ablation of dental tissues [165, 182], thus offering attractive options for laser dentistry.

8.4 Photonic-crystal fibers with a large hollow core: transmission and transformation of subgigawatt femtosecond laser pulses

The transmission and control of high-power ultrashort laser pulses are the key problems in physics of high radiation fields and laser technologies. Self-focusing and optical breakdown limit the use of standard optical fibers for these applications. Hollow fibers with a solid cladding [21] radically enhance nonlinear-optical interactions [18], allowing the formation of ultrashort light pulses [183, 184] and providing high efficiencies of high-order harmonic generation [185, 186]. Such fibers are, however, intrinsically multimode and offer only limiting options for broadband dispersion control.

Hollow-core PCFs with tailored dispersion profiles are ideally suited to solving these problems, allowing control of the pulse width and temporal shape of high-power ultrashort laser pulses [163]. Hollow-core PCFs designed for the transmission and nonlinear-optical transformation of high-power ultrashort laser pulses [187] have a period of photonic-crystal cladding of about 5 μm and a core diameter of approximately 50 μm (the inset to Fig. 18a). Transmission spectra of these fibers display characteristic well-pronounced isolated passbands related to the photonic band gaps or bands of low density of photonic states provided by the microstructured cladding.

The guided modes and transmission spectra of the considered type of hollow PCFs were modelled by a numerical solution of the wave equations for the transverse components of the electric field through the expansion of the field and the refractive-index profile based on orthogonal polynomials. With such an expansion, the solution of the wave equation with the relevant boundary conditions is reduced to an eigenfunction and eigenvalue problem of a matrix equation for the expansion coefficients [172, 173]. Lines *1* and *2* in Fig. 18a represent the effective mode index $n_{\mathrm{eff}} - 1$ and the GVD as the functions of the radiation wavelength for the fundamental mode of a hollow PCF with the cross-section structure shown in the inset to this figure.

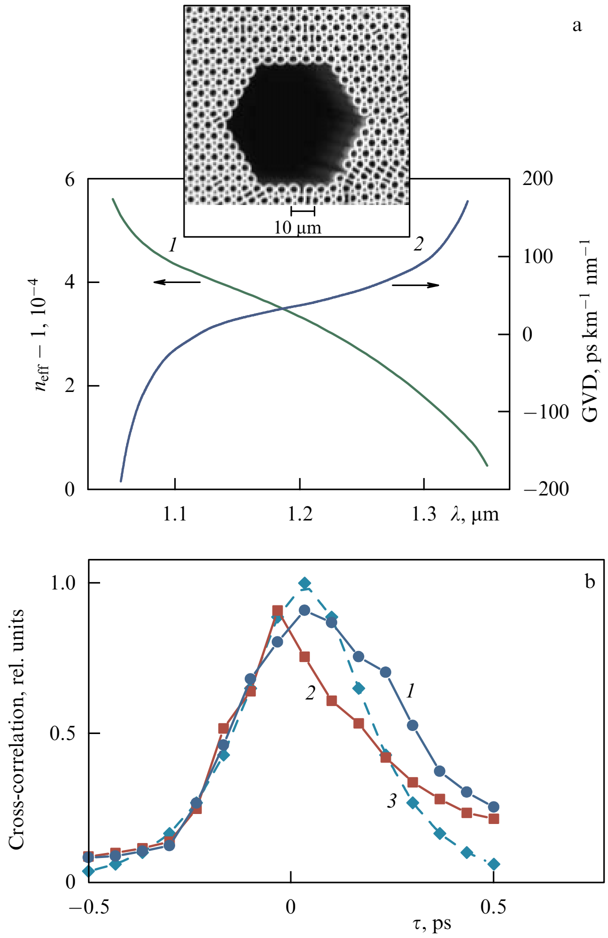

Figure 18. (a) The effective mode index $n_{\mathrm{eff}} - 1$ and the group-velocity dispersion D as functions of the radiation wavelength for the fundamental mode of the hollow PCF with the cross-section structure shown in the inset. (b) Cross-correlation traces for Cr:forsterite-laser pulses at the output of the hollow PCF (*1*, *2*) and at the output of the laser system (*3*). The energy of the laser pulse at the input of the PCF is 50 nJ (*1*) and 35 μJ (*2*).

The calculated results presented in Fig. 18a show that the considered hollow PCF provides an anomalous GVD ($D > 0$) within a sufficiently broad spectral range, including the fundamental wavelength of Cr:forsterite-laser radiation (1.25 μm). Such a fiber allows a self-compression of Cr:forsterite-laser pulses due to the GVD compensation for the chirp of these pulses, induced by self-phase modulation in the hollow-core of a PCF filled with a gas having a nonlinear refractive index $n_2 > 0$.

In experiments [163], a standard micro-objective served to couple amplified Cr:forsterite-laser pulses [148] into a hollow PCF filled with atmospheric air and placed on a three-dimensional translation stage. Beam coupling was optimized to provide the maximum efficiency of fundamental-mode excitation in the PCF. The input laser pulses had an initial duration of about 270 fs (the dashed line in Fig. 18b) and an energy ranging from 10 nJ up to 50 μJ.

A cross-correlation technique was used to measure the temporal envelope and the duration of laser pulses transmitted through the hollow PCF. The signal coming out of the PCF was mixed with a fundamental-wavelength reference Cr:forsterite-laser pulse in a BBO crystal with a thickness of about 1 mm. The resulting sum-frequency signal was measured as a function of the delay time between the signal and the reference pulse to yield the cross-correlation trace. The results of cross-correlation measurements are presented in Fig. 18b. In the regime of low intensities, the laser pulses increase their pulse width as they propagate through the PCF. Pulses with an initial duration of about 270 fs and an energy of 50 nJ lengthen up to approximately 350 fs as they reach the output of the fiber with a length of 9 cm (curve *1* in Fig. 18b). High-intensity laser pulses experience self-phase modulation due to the Kerr nonlinearity of the gas filling the hollow core of the PCF. The characteristic length $L_{\rm nl}$ for this nonlinear-optical process is determined by the coefficient of nonlinearity

$$\gamma = \frac{n_2 \omega}{c S_{\rm eff}} \,,$$

where $S_{\rm eff}$ is the effective area of the waveguide mode, and the power P of the laser pulse:

$$L_{\rm nl} = (\gamma P)^{-1} \,.$$

For laser pulses with a wavelength of 1.25 μm, an initial duration of 270 fs and an energy of 35 μJ, the characteristic length $L_{\rm nl} \approx 6.3$ cm of self-phase modulation in a hollow PCF filled with atmospheric air at the pressure $p = 1$ atm ($n_2 \approx 5 \times 10^{-19}$ cm^2 W^{-1}) is less than the chosen PCF length. Optical nonlinearity of the gas in the fiber core under these conditions gives rise to a noticeable chirp of the laser pulse.

In the regime of anomalous dispersion provided by the hollow PCF, laser pulses experience a nonuniform frequency deviation, and their duration decreases. The typical duration of a laser pulse with a power $P \approx 130$ MW at the output of the PCF is about 210 fs (curve *2* in Fig. 18b). High-order dispersion noticeably distorts the output pulse. Comparison of curves *1* and *2* in Fig. 18b shows that the highest efficiency of pulse compression is achieved around the peak of the laser pulse, where the laser intensity reaches its maximum. Off the laser pulse peak, the radiation intensity is lower, and optical nonlinearity is smaller. As a result, pulse edges virtually coincide for low- and high-intensity pulses (see Fig. 18b). A further increase in the input energy of laser pulses results in a considerable distortion of output pulses. This tendency can be attributed to the ionization nonlinearity of the gas filling the fiber core, as well as the solitonic effects.

Experimental studies [163] thus suggest that hollow PCFs with a special dispersion profile can efficiently control the duration and the waveform of high-power ultrashort laser pulses. This option is illustrated by the experimental demonstration of a waveguide self-compression of ultrashort pulses with a power exceeding 100 MW. One can expect that dispersion optimization of hollow PCFs, extended to include high-order dispersion terms, multisoliton interactions, and ionization nonlinearity, should allow the creation of efficient fiber-optic compressors and transmission lines for high-power ultrashort laser pulses.

9. Conclusion

Recent developments in fiber optics, including the creation of novel types of optical fibers, are based on the latest achievements in optical technologies combined with new ideas and advanced approaches in ultrafast science, the optics of micro- and nanostructures, the physics of photonic crystals, and nonlinear guided-wave optics. Photonic-crystal fibers are playing a progressively significant role in the creation of compact and efficient fiber-optic systems for the generation and control of ultrashort light pulses. Dispersion and field-profile tailoring is the key advantage of photonic-crystal fibers, which allows a high-precision dispersion balance to be achieved within a broad spectral range, enabling the creation of novel types of fiber-optic sources of ultrashort light pulses. Methods used in nano-optics help to tailor dispersion profiles of PCF modes, providing a highly efficient frequency conversion of femtosecond laser pulses and enabling the wavelength-tunable generation of broad-band radiation. Special strategies of micro- and nanostructuring of the core and the cladding of optical fibers help to realize an efficient spectral and temporal transformation of laser pulses with input pulse widths from dozens of nanoseconds down to several field cycles within the range of peak powers from hundreds of watts up to several gigawatts. Hollow-core photonic-crystal fibers supporting soliton transmission regimes for megawatt pulses open up new possibilities in laser biomedicine and optical technologies.

Acknowledgments. I am pleased to gratefully acknowledge fruitful collaboration and illuminating discussions with A B Fedotov, D A Sidorov-Biryukov, E E Serebryannikov, I V Fedotov, A V Mitrofanov, R R Musin, A A Podshivalov, A D Savin, and V P Mitrokhin (Physics Department, M V Lomonosov Moscow State University); A A Ivanov and M V Alfimov (Center of Photochemistry, Russian Academy of Sciences); A Baltuska and E Wintner (Technological University of Vienna); A Apolonskii and F Krausz (Max Planck Institute for Quantum Optics, Garching); R Miles and M Sheider (Princeton University); A Galvanauskas (University of Michigan); D von der Linde and A P Tarasevitch (University of Essen — Duisburg); P St J Russell (University of Erlangen — Nürnberg), J C Knight (University of Bath); Yu N Kondrat'ev, V S Shevandin, K V Dukel'skii, and A V Khokhlov (S I Vavilov State Optical Institute, St.-Petersburg); V I Beloglazov, N B Skibina, and A V Shcherbakov (Institute of Technology and Equipment for Glass Structures, Saratov); D Chorvat, I Bugar, and F Uherek (International Laser Center, Bratislava); Ching-yue Wang, Minglie Hu, and Yanfeng Li (Tianjin University), and L A Mel'nikov (N G Chernyshevsky Saratov State University).

This study was supported in part by the Russian Foundation for Basic Research (project Nos 06-02-16880 and 05-02-90566-NNS), the Russian Federal Research and Technology Program (contract No. 02.434.11.2010), and INTAS (project Nos 03-51-5037 and 03-51-5288). The research described in this publication was made possible in part by award No. RUP2-2695 of the U.S. Civilian Research & Development Foundation for the Independent States of the Former Soviet Union (CRDF).

References

1. Payne D N, in *Fiber Lasers: The Next Generation, Plenary Lecture at the Conf. on Lasers and Electro-Optics* (*CLEO2006*), *Long Beach, CA, 2006*
2. Agrawal G P *Nonlinear Fiber Optics* 3rd ed. (San Diego: Academic Press, 2001)
3. Strickland D, Mourou G *Opt. Commun.* **56** 219 (1985)
4. Limpert J et al. *Opt. Lett.* **28** 1984 (2003)
5. Liem A et al. *Appl. Phys. B* **71** 889 (2000)
6. Galvanauskas A *IEEE J. Sel. Top. Quantum Electron.* **7** 504 (2001)

7. Duling I N III *Electron. Lett.* **27** 544 (1991)
8. Tamura K et al. *Opt. Lett.* **18** 1080 (1993)
9. Knight J C et al. *Opt. Lett.* **21** 1547 (1996)
10. Knight J C et al. *Science* **282** 1476 (1998)
11. Russell P *Science* **299** 358 (2003)
12. Knight J C *Nature* **424** 847 (2003)
13. Zheltikov A M *Optika Mikrostrukturirovannykh Volokon* (Optics of Microstructure Fibers) (Moscow: Nauka, 2004)
14. Russell P St J *J. Lightwave Technol.* **24** 4729 (2006)
15. Cregan R F et al. *Science* **285** 1537 (1999)
16. Konorov S O et al. *Pis'ma Zh. Eksp. Teor. Fiz.* **76** 401 (2002) [*JETP Lett.* **76** 341 (2002)]
17. Smith C M et al. *Nature* **424** 657 (2003)
18. Zheltikov A M *Usp. Fiz. Nauk* **174** 1301 (2004) [*Phys. Usp.* **47** 1205 (2004)]
19. Luan F et al. *Opt. Lett.* **29** 2369 (2004)
20. Zheltikov A M *Nature Mater.* **4** 267 (2005)
21. Marcatili E A J, Schmeltzer R A *Bell Syst. Tech. J.* **43** 1783 (1964)
22. Adams M J *An Introduction to Optical Waveguides* (Chichester: Wiley, 1981)
23. Ferrando A et al. *Opt. Express* **9** 687 (2001)
24. Ferrando A et al. *Opt. Lett.* **25** 790 (2000)
25. Reeves W H et al. *Opt. Express* **10** 609 (2002)
26. Reeves W H et al. *Nature* **424** 511 (2003)
27. Skryabin D V et al. *Science* **301** 1705 (2003)
28. Zheltikov A M *Phys. Rev. A* **72** 043812 (2005)
29. Zheltikov A M *Usp. Fiz. Nauk* **174** 73 (2004) [*Phys. Usp.* **47** 69 (2004)]
30. Ranka J K, Windeler R S, Stentz A J *Opt. Lett.* **25** 25 (2000)
31. Wadsworth W J et al. *J. Opt. Soc. Am. B* **19** 2148 (2002)
32. Zheltikov A M (Ed.) "Supercontinuum generation" *Appl. Phys. B* **77** (Special issue 2/3) (2003)
33. Zheltikov A M *Usp. Fiz. Nauk* **176** 623 (2006) [*Phys. Usp.* **49** 605 (2006)]
34. Dudley J M, Genty G, Coen S *Rev. Mod. Phys.* **78** 1135 (2006)
35. Jones D J et al. *Science* **288** 635 (2000)
36. Holzwarth R et al. *Phys. Rev. Lett.* **85** 2264 (2000)
37. Diddams S A et al. *Phys. Rev. Lett.* **84** 5102 (2000)
38. Udem Th, Holzwarth R, Hänsch T W *Nature* **416** 233 (2002)
39. Serebryannikov E E et al. *Phys. Rev. E* **72** 056603 (2005)
40. Teisset C et al. *Opt. Express* **13** 6550 (2005)
41. Hartl I et al. *Opt. Lett.* **26** 608 (2001)
42. Konorov S O et al. *Phys. Rev. E* **70** 057601 (2004)
43. Sidorov-Biryukov D A, Serebryannikov E E, Zheltikov A M *Opt. Lett.* **31** 2323 (2006)
44. Paulsen H N et al. *Opt. Lett.* **28** 1123 (2003)
45. Kano H, Hamaguchi H *Opt. Express* **13** 1322 (2005)
46. von Vacano B, Wohlleben W, Motzkus M *Opt. Lett.* **31** 413 (2006)
47. Lim H, Ilday F, Wise F *Opt. Express* **10** 1497 (2002)
48. Chen X et al. *Opt. Express* **12** 3888 (2004)
49. Lim H, Chong A, Wise F W *Opt. Express* **13** 3460 (2005)
50. Isomäki A, Okhotnikov O G *Opt. Express* **14** 4368 (2006)
51. Sharping J E et al. *Opt. Lett.* **27** 1675 (2002)
52. de Matos C J S, Taylor J R, Hansen K P *Opt. Lett.* **29** 983 (2004)
53. Deng Y et al. *Opt. Lett.* **30** 1234 (2005)
54. Sharping J et al. *Opt. Express* **12** 3086 (2004)
55. Rarity J et al. *Opt. Express* **13** 534 (2005)
56. Birks T A, Knight J C, Russell P St J *Opt. Lett.* **22** 961 (1997)
57. Knight J C et al. *Electron. Lett.* **34** 1347 (1998)
58. Furusawa K et al. *Opt. Express* **9** 714 (2001)
59. Wadsworth W J et al. *Electron. Lett.* **36** 1452 (2000)
60. Furusawa K et al. *Electron. Lett.* **37** 560 (2001)
61. Wadsworth W et al. *Opt. Express* **11** 48 (2003)
62. Limpert J et al. *Opt. Express* **11** 818 (2003)
63. Südmeyer T et al. *Opt. Lett.* **28** 1951 (2003)
64. Mitrofanov A V et al. *Pis'ma Zh. Eksp. Teor. Fiz.* **85** 283 (2007) [*JETP Lett.* **85** 231 (2007)]
65. Mitrokhin V P et al. *Laser Phys. Lett.* (in press)
66. Pickrell G, Peng W, Wang A *Opt. Lett.* **29** 1476 (2004)
67. Jensen J B et al. *Opt. Lett.* **29** 1974 (2004)
68. Konorov S, Zheltikov A, Scalora M *Opt. Express* **13** 3454 (2005)
69. Marcatili E A J, Schmeltzer R A *Bell Syst. Tech. J.* **43** 1783 (1964)
70. Limpert J et al. *Opt. Express* **11** 3332 (2003)
71. de Matos C J S et al. *Phys. Rev. Lett.* **93** 103901 (2004)
72. Serebryannikov E E, Zheltikov A M et al. (submitted)
73. Monro T M et al. *J. Lightwave Technol.* **18** 50 (2000)
74. Serebryannikov E E, von der Linde D, Zheltikov A M *Phys. Rev. E* **70** 066619 (2004)
75. Haupt R L, Haupt S E *Practical Genetic Algorithms* 2nd ed. (Hoboken, NJ: John Wiley, 2004)
76. Poletti F et al. *Opt. Express* **13** 3728 (2005)
77. Kerrinckx E et al. *Opt. Express* **12** 1990 (2004)
78. Musin R R, Zheltikov A M (submitted)
79. Saitoh K, Koshiba M *IEEE J. Quantum Electron.* **38** 927 (2002)
80. Saitoh K, Florous N, Koshiba M *Opt. Express* **13** 8365 (2005)
81. Saitoh K, Florous N J, Koshiba M *Opt. Lett.* **31** 26 (2006)
82. Zheltikov A M *Appl. Phys. B* **84** 69 (2006)
83. Serebryannikov E E, Zheltikov A M *J. Opt. Soc. Am. B* **23** 1700 (2006)
84. Li Y-F et al. *Opt. Express* **14** 10878 (2006)
85. Fedotov A B et al. *Appl. Opt.* **45** 6823 (2006)
86. Zheltikov A M *Opt. Commun.* **270** 402 (2007)
87. Akhmediev N, Karlsson M *Phys. Rev. A* **51** 2602 (1995)
88. Dianov E M et al. *Pis'ma Zh. Eksp. Teor. Fiz.* **41** 242 (1985) [*JETP Lett.* **41** 294 (1985)]
89. Mitschke F M, Mollenauer L F *Opt. Lett.* **11** 659 (1986)
90. Liu X et al. *Opt. Lett.* **26** 358 (2001)
91. Washburn B R et al. *Electron. Lett.* **37** 1510 (2001)
92. Price J H V et al. *J. Opt. Soc. Am. B* **19** 1286 (2002)
93. Cormack I G et al. *Electron. Lett.* **38** 167 (2002)
94. Abedin K S, Kubota F *Opt. Lett.* **28** 1760 (2003)
95. Serebryannikov E E et al. *Appl. Phys. B* **81** 585 (2005)
96. Ishii N et al. *Phys. Rev. E* **74** 036617 (2006)
97. Gordon J P *Opt. Lett.* **11** 662 (1986)
98. Stolen R H et al. *J. Opt. Soc. Am. B* **6** 1159 (1989)
99. Mamyshev P V, Chernikov S V *Opt. Lett.* **15** 1076 (1990)
100. Kibler B, Dudley J M, Coen S *Appl. Phys. B* **81** 337 (2005)
101. Santhanam J, Agrawal G P *Opt. Commun.* **222** 413 (2003)
102. Serebryannikov E E, Zheltikov A M *J. Opt. Soc. Am. B* **23** 1882 (2006)
103. Zheltikov A M *Phys. Rev. E* **75** 037603 (2007)
104. Serebryannikov E E et al. *Phys. Rev. E* **73** 066617 (2006)
105. Shen Y R *The Principles of Nonlinear Optics* (New York: J. Wiley, 1984)
106. Guenther R D (Ed.-in-Chief), Steel D G, Bayvel L (Eds) *Encyclopedia of Modern Optics* (Amsterdam: Elsevier/Academic Press, 2005)
107. Zheltikov A M *Sverkhkorotkie Impul'sy i Metody Nelineinoi Optiki* (Ultrashort Pulses and Methods of Nonlinear Optics) (Moscow: Nauka, 2006)
108. Ranka J K, Windeler R S, Stentz A J *Opt. Lett.* **25** 796 (2000)
109. Omenetto F G et al. *Opt. Lett.* **26** 1158 (2001)
110. Omenetto F et al. *Opt. Express* **11** 61 (2003)
111. Efimov A et al. *Opt. Express* **11** 910 (2003)
112. Efimov A et al. *Opt. Express* **11** 2567 (2003)
113. Zheltikov A M *Phys. Rev. A* **72** 043812 (2005)
114. Ivanov A A et al. *Phys. Rev. E* **73** 016610 (2006)
115. Naumov A N et al. *J. Opt. Soc. Am. B* **19** 2183 (2002)
116. Akimov D A et al. *Appl. Phys. B* **76** 515 (2003)
117. Serebryannikov E E et al. *J. Opt. Soc. Am. B* **23** 1975 (2006)
118. Zheltikov A M *J. Opt. Soc. Am. B* **22** 2263 (2005)
119. Fedotov A B et al. *Phys. Rev. E* **75** 016614 (2007)
120. Yulin A V, Skryabin D V, Russell P St J *Opt. Lett.* **29** 2411 (2004)
121. Skryabin D V, Yulin A V *Phys. Rev. E* **72** 016619 (2005)
122. Efimov A et al. *Opt. Express* **12** 6498 (2004)
123. Biancalana F, Skryabin D V, Yulin A V *Phys. Rev. E* **70** 016615 (2004)
124. Coen S et al. *J. Opt. Soc. Am. B* **19** 753 (2002)
125. Dudley J M et al. *J. Opt. Soc. Am. B* **19** 765 (2002)
126. Genty G, Ritari T, Ludvigsen H *Opt. Express* **13** 8625 (2005)
127. Avdokhin A V, Popov S V, Taylor J R *Opt. Lett.* **28** 1353 (2003)
128. Travers J C et al. *Opt. Lett.* **30** 1938 (2005)
129. Herrmann J et al. *Phys. Rev. Lett.* **88** 173901 (2002)
130. Bowden C M, Zheltikov A M (Eds) "Nonlinear optics of photonic crystals" *J. Opt. Soc. Am. B* **19** (Feature issue 9) (2002)
131. Shen Y R, Bloembergen N *Phys. Rev.* **137** A1787 (1965)

132. Fedotov I V et al. *Ross. Nanotekhnol.* (in press)
133. Alfimov M V et al. *Pis'ma Zh. Eksp. Teor. Fiz.* **71** 714 (2000) [*JETP Lett.* **71** 489 (2000)]
134. Zheltikov A M *Kvantovaya Elektron.* **32** 542 (2002) [*Quantum Electron.* **32** 542 (2002)]
135. Zheltikov A M *Usp. Fiz. Nauk* **170** 1203 (2000) [*Phys. Usp.* **43** 1125 (2000)]
136. Zheltikov A M *Opt. Spektrosk.* **95** 440 (2003) [*Opt. Spectrosc.* **95** 410 (2003)]
137. Akimov D A et al. *Opt. Lett.* **28** 1948 (2003)
138. Magi E, Steinvurzel P, Eggleton B *Opt. Express* **12** 776 (2004)
139. Leon-Saval S et al. *Opt. Express* **12** 2864 (2004)
140. Lizé Y et al. *Opt. Express* **12** 3209 (2004)
141. Foster M, Moll K, Gaeta A *Opt. Express* **12** 2880 (2004)
142. Foster M, Gaeta A *Opt. Express* **12** 3137 (2004)
143. Foster M et al. *Opt. Express* **13** 6848 (2005)
144. Zheltikov A *J. Opt. Soc. Am. B* **22** 1100 (2005)
145. Zheltikov A M *Opt. Commun.* **252** 78 (2005)
146. Lenzner M et al. *Phys. Rev. Lett.* **80** 4076 (1998)
147. Mitrofanov A V et al. (submitted)
148. Ivanov A A, Alfimov M V, Zheltikov A M *Usp. Fiz. Nauk* **174** 743 (2004) [*Phys. Usp.* **47** 687 (2004)]
149. Linden S, Kuhl J, Giessen H *Opt. Lett.* **24** 569 (1999)
150. Gu X et al. *Opt. Lett.* **27** 1174 (2002)
151. Schenkel B, Paschotta R, Keller U *J. Opt. Soc. Am. B* **22** 687 (2005)
152. Hasegawa A *Optical Solitons in Fibers* (Berlin: Springer-Verlag, 1990)
153. Kivshar Y S, Agrawal G P *Optical Solitons: From Fibers to Photonic Crystals* (Amsterdam: Academic Press, 2003)
154. Zheltikov A M *Usp. Fiz. Nauk* **172** 743 (2002) [*Phys. Usp.* **45** 687 (2002)]
155. Benabid F et al. *Science* **298** 399 (2002)
156. Konorov S O, Fedotov A B, Zheltikov A M *Opt. Lett.* **28** 1448 (2003)
157. Benabid F et al. *Nature* **434** 488 (2005)
158. Konorov S O et al. *Phys. Rev. A* **70** 023807 (2004)
159. Konorov S O et al. *Appl. Phys. Lett.* **85** 3690 (2004)
160. Konorov S O et al. *Phys. Rev. E* **70** 066625 (2004)
161. Ouzounov D G et al. *Science* **301** 1702 (2003)
162. Ouzounov D et al. *Opt. Express* **13** 6153 (2005)
163. Konorov S O et al. *Pis'ma Zh. Eksp. Teor. Fiz.* **81** 65 (2005) [*JETP Lett.* **81** 58 (2005)]
164. Ivanov A A, Podshivalov A A, Zheltikov A M *Opt. Lett.* **31** 3318 (2006)
165. Konorov S O et al. *Appl. Opt.* **43** 2251 (2004)
166. Konorov S O et al. *J. Phys. D: Appl. Phys.* **36** 1375 (2003)
167. Shephard J et al. *Opt. Express* **12** 717 (2004)
168. Flusberg B A et al. *Opt. Lett.* **30** 2272 (2005)
169. Fu L et al. *Opt. Express* **14** 1027 (2006)
170. Ritari T et al. *Opt. Express* **12** 4080 (2004)
171. Zheltikov A M *Ross. Nanotekhnol.* **2** (5–6) 50 (2007)
172. Poladian L, Issa N, Monro T *Opt. Express* **10** 449 (2002)
173. Konorov S O et al. *Phys. Rev. E* **71** 057603 (2005)
174. Bessonov A D, Zheltikov A M *Phys. Rev. E* **73** 066618 (2006)
175. Koenig K et al. *Cell. Mol. Biol.* **45** 192 (1999)
176. Juhasz T et al. *IEEE J. Sel. Topics Quantum Electron.* **5** 902 (1999)
177. Konig K, Riemann I, Fritzsche W *Opt. Lett.* **26** 819 (2001)
178. Shen N et al., in *Technical Digest: Summaries of Papers Presented at the Conf. on Lasers and Electro-Optics* (OSA Trends in Optics and Photonics, Vol. 56) (Washington, DC: Optical Society of America, 2001) p. 403
179. Tsai P S et al. *Neuron* **39** 27 (2003)
180. Neev J et al. *Proc. SPIE* **2672** 250 (1996)
181. Rubenchik A M et al. *Proc. SPIE* **2672** 222 (1996)
182. Konorov S O et al. *Phys. Med. Biol.* **49** 1359 (2004)
183. Nisoli M, De Silvestri S, Svelto O *Appl. Phys. Lett.* **68** 2793 (1996)
184. Zhavoronkov N, Korn G *Phys. Rev. Lett.* **88** 203901 (2002)
185. Constant E et al. *Phys. Rev. Lett.* **82** 1668 (1999)
186. Paul A et al. *Nature* **421** 51 (2003)
187. Konorov S O et al. *Laser Phys. Lett.* **1** 548 (2004)